International Journal of
Molecular Sciences

MDPI

Article

Aberrant STING Signaling Links FGFR1 Deficiency to Cardiac Inflammation

Sanskruti R. Gare [1,†], Yihua Han [1,†], Min Fang [1], Nasser H. Alatawi [1], Claire Ross [1], Oveena Fonseka [1], Xinyi Chen [1], Jiayan Zhang [1], Riham R. E. Abouleisa [2], Tao Wang [1], Sabu Abraham [1], Gareth Howell [1], Tamer M. A. Mohamed [1,2,3], Bernard D. Keavney [1,3,4] and Wei Liu [1,*]

[1] Core Technology Facility, Faculty of Biology, Medicine and Health, The University of Manchester, Manchester M13 9WU, UK
[2] Surgery Department, Baylor College of Medicine, Houston, TX 77030, USA
[3] Institute of Molecular Cardiology, University of Louisville, Louisville, KY 40202, USA
[4] Manchester Heart Centre, Manchester University NHS Foundation Trust, Manchester Academic Health Science Centre, Manchester M13 9WL, UK
* Correspondence: wei.liu@manchester.ac.uk
† These authors contributed equally to this work.

Abstract

Diabetes is a major risk factor for heart failure (HF) and is closely associated with chronic myocardial inflammation, yet the molecular mechanisms underlying myocardial inflammatory signaling remain incompletely understood. This study aimed to investigate the role of fibroblast growth factor receptor 1 (FGFR1) in regulating cardiac inflammation under diabetic conditions. Proteomic and transcriptomic analyses of human and mouse diabetic failing hearts revealed significant activation of inflammatory pathways accompanied by reduced FGFR1 expression. Diabetic human hearts showed increased tumor necrosis factor alpha (TNF-α) expression and a shift toward pro-inflammatory M1 macrophage polarization. To establish causality, cardiomyocyte-specific FGFR1 knockout ($FGFR1^{cKO}$) mice were subjected to a high-fat, high-sucrose diet combined with low-dose streptozotocin. FGFR1 deficiency led to worsened cardiac dysfunction and enhanced NF-κB expression. Mechanistically, loss of FGFR1 suppressed AKT phosphorylation at Ser473, promoting stimulator of interferon genes (STING) translocation and subsequent nuclear factor kappa-light-chain-enhancer of activated B cells (NF-κB)-mediated TNF-α production. Cardiomyocyte-derived TNF-α was associated with pro-inflammatory macrophage polarization, which was reversed by protein kinase B activation or STING inhibition. Importantly, cardiomyocyte-specific restoration of FGFR1 via AAV9-mediated gene delivery reduced cardiac inflammation and improved cardiac function. These findings identify FGFR1 as an anti-inflammatory regulator that limits STING-NF-κB signaling and represents a potential therapeutic target in diabetic HF.

Keywords: heart failure; diabetes; inflammation; FGFR1

Check for updates

Academic Editor: Claudia Kusmic

Received: 21 October 2026
Revised: 18 November 2026
Accepted: 20 November 2026
Published: 24 November 2026

Copyright: © 2026 by the authors. Licensee MDPI, Basel, Switzerland. This article is an open access article distributed under the terms and conditions of the Creative Commons Attribution (CC BY) license.

1. Introduction

Diabetes mellitus is a major contributor to cardiovascular disease and is strongly associated with myocardial structural and functional abnormalities. Molecular disturbances including chronic cardiac inflammation, directly promote myocardial dysfunction, leading to diabetic cardiomyopathy and increased risk of heart failure (HF) [1]. Clinical data demonstrate that diabetes predisposes to HF, underscoring the need for targeted therapeutic strategies [2].

Local cardiac inflammation is a key pathogenic mechanism linking diabetes to the development of HF. Chronic diabetic conditions activate innate immune signaling within the myocardium, leading to the upregulation of pro-inflammatory cytokines, including tumor necrosis factor-alpha (TNF-α), IL-1β and IL-6, and increased infiltration of inflammatory cells [3]. These inflammatory mediators further drive maladaptive cardiac remodeling and impair molecular homeostasis in cardiomyocytes. Over time, sustained inflammatory signaling promotes structural and functional deterioration, compromising ventricular diastolic and systolic performance, ultimately culminating in HF. Targeting myocardial inflammatory pathways therefore represents a promising therapeutic strategy to prevent or attenuate diabetic cardiomyopathy and its progression to HF [4].

Fibroblast growth factor receptor 1 (FGFR1) is a receptor tyrosine kinase that mediates fibroblast growth factor (FGF) signaling and regulates cell proliferation, differentiation, and survival. It also plays critical roles in inflammatory signaling. FGFR1 is positively correlated with inflammatory responses in macrophages and cancer cells [5–7]; in contrast, its deficiency promotes inflammation in endothelial cells [8]. We have found that FGFR1 overexpression in myoblasts suppresses inflammatory factors; however, its function in the heart under diabetic stress is unexplored.

Stimulator of interferon genes (STING) is a central mediator of innate immune signaling under pathological stresses [9]. STING's role is increasingly being recognized in cardiovascular diseases. Aberrant cardiac STING activation promotes myocardial inflammation [10,11] as well as pathological cardiac remodeling [12,13], contributing to CM injury and cardiomyopathy. Similarly, chronic diabetic stress-induced STING activation in CMs leads to myocardial inflammation [14,15] and diabetic cardiomyopathy, which highlights the therapeutic potential of targeting STING in HF.

STING is activated when cytosolic DNA, often from damaged mitochondria or nuclei, is sensed by cyclic GMP-AMP synthase (cGAS). Upon activation, STING translocates from the endoplasmic reticulum (ER) to the Golgi apparatus, where it initiates downstream signaling cascades, leading to the activation of nuclear factor kappa-light-chain-enhancer of activated B cells (NF-κB) and the subsequent induction of type I interferons (IFNs) and pro-inflammatory cytokines [16,17]. Several kinases act as modulators, amplifiers, or negative regulators during this process, shaping the amplitude and duration of the STING response [18]. It remains unknown whether FGFR1 regulates STING activation, particularly in the heart.

In this study, we first demonstrate that in human and mouse diabetic failing hearts, FGFR1 reduction was associated with myocardial inflammation. Furthermore, we found that mice with cardiomyocyte-specific FGFR1 deficiency exhibited exacerbated myocardial inflammation, contributing to cardiac dysfunction under diabetic stress. FGFR1 loss attenuated the phosphorylation of protein kinase B (AKT), subsequently promoting STING-elevated cardiac cytokines including TNF-α. Most importantly, cardiomyocyte FGFR1 restoration attenuated the inflammatory response in the myocardium. These data reveal that cardiac FGFR1 is required to suppress inflammation in the diabetic heart.

2. Results

2.1. Inflammatory Pathways Are Altered in Diabetic Hearts

Consistent with the notion that HF is associated with pro-inflammatory changes, mass spectrometry followed by Gene Ontology (GO) pathway (Reactome) enrichment analysis on 358 altered proteins ($p < 0.05$) revealed alterations in inflammatory pathways and cytokine-mediated pathways ($p < 0.05$) (Figure 1A) in human failing hearts. Since diabetes is a high-risk factor inducing HF and inflammatory condition, human diabetic failing hearts displayed an increased abundance of $CD86^+$ macrophages, a marker of pro-inflammatory

M1 macrophages (Figure 1B), accompanied by a reduction in CD206$^+$ macrophages, indicative of anti-inflammatory M2 macrophages (Figure 1C). In line with the observations from human tissues, RNA sequencing analyses performed on hearts from mice subjected to 12 weeks of HFHSD combined with STZ, imitating the late stage of type 2 diabetic stress, showed a similar phenomenon. GO analyses on 2771 differentially expressed genes ($P_{adj.} < 0.05$; absolute $Log_2FC > 1$) also demonstrated dysregulated inflammatory pathways and cytokine-mediated pathways ($p < 0.05$) (Figure 1D), supporting a link between myocardial inflammation and diabetic HF.

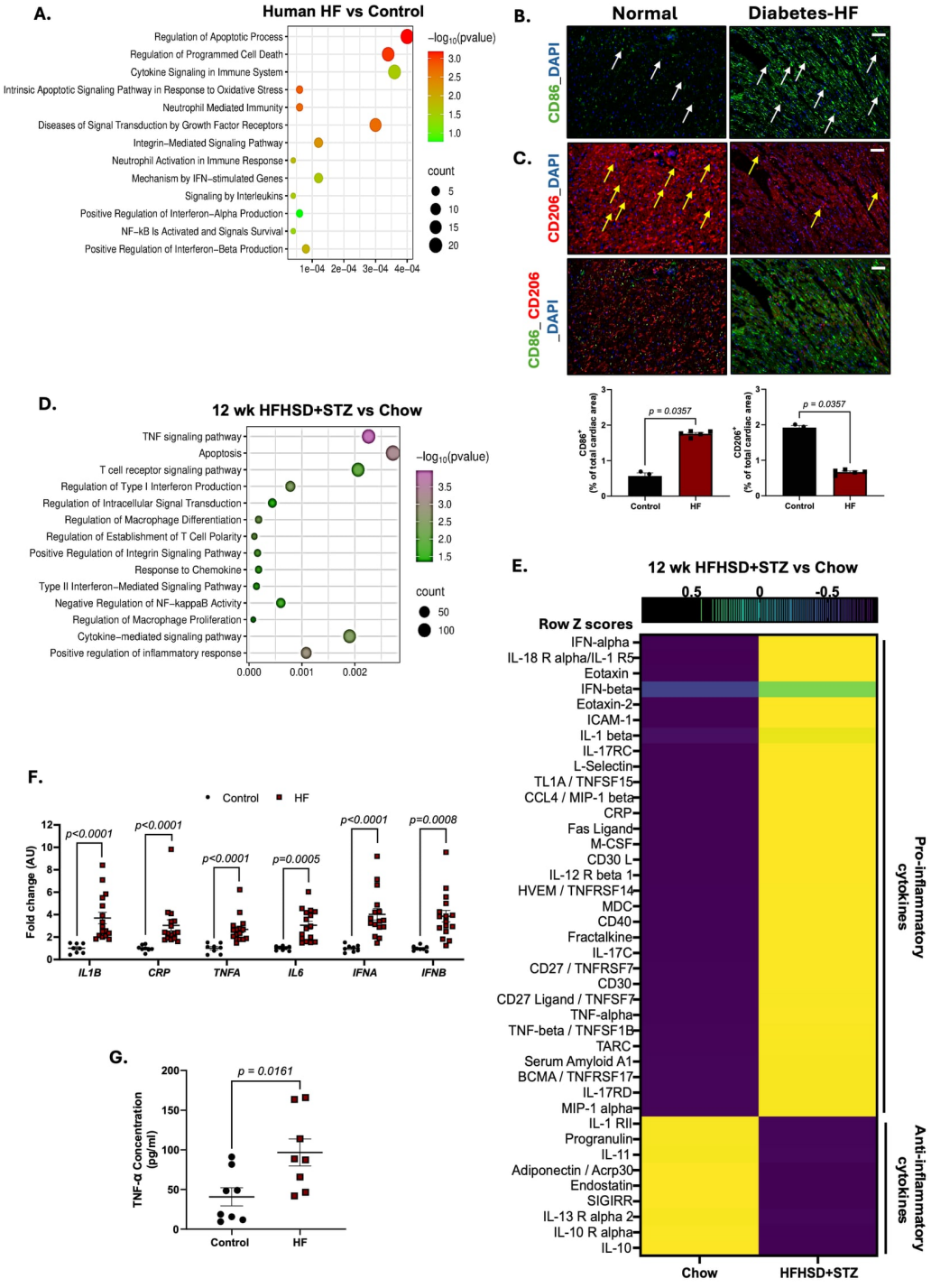

Figure 1. Human and mouse diabetic failing hearts exhibit heightened inflammation and reduced FGFR1 expression. (**A**) Gene Ontology (GO) and Reactome pathway enrichment analyses of the differentially

expressed proteins ($p < 0.05$) identified via liquid chromatography–tandem mass spectrometry of human diabetic failing hearts versus healthy controls ($n = 8$ hearts for control group, 14 hearts for HF group). (**B**,**C**) Immunofluorescent co-staining with CD86 (green, white arrows), CD206 (red, yellow arrows) with DAPI (blue) and merged staining in human heart tissues with quantification of $CD86^+$ and $CD206^+$ area ($n = 3$ hearts for control group, 5 hearts for diabetes associated HF group; scale bar = 20 µm). (**D**) GO pathway enrichment analyses of the differentially expressed genes ($P_{adj.} < 0.05$; absolute $Log_2FC > 1$) identified via RNA sequencing in mouse hearts subjected to a 12-week high-fat, high-sucrose diet (HFHSD) and streptozotocin (STZ) injections compared to chow-fed mice ($n = 4$ mice of both sexes/group). (**E**) Heatmap of cytokine array analysis showing differentially expressed cytokines ($q < 0.05$) in mouse hearts following 12-week HFHSD + STZ stress compared to chow-fed controls (n = 2 pooled samples, each including 4 hearts of both sexes/group). (**F**) Quantitative PCR analysis of *IL1B*, *CRP, TNFA*, *IL6*, IFNA and *IFNB* in human diabetic failing hearts ($n = 8$ hearts for control group, 14 hearts for HF group). Each gene was analyzed separately, with expression normalized to *PGK1* and expressed as fold change relative to the corresponding human control group. (**G**) TNF-α protein levels measured by ELISA in human diabetic failing hearts versus controls ($n = 8$ hearts for control group, 14 hearts for HF group). Data are presented as the mean ± SEM. Statistical significance (p values shown in the panel) was assessed using the Mann–Whitney U test (**B**,**C**), unpaired t-test (**F**,**G**) and multiple unpaired t-tests (**E**).

Interestingly, GO pathway analyses also revealed impaired growth factor receptor signal transduction ($p < 0.05$) in human failing hearts (Figure 1A). Previously, we showed that enhanced FGFR1 signaling in myoblasts increases the secretion of anti-inflammatory cytokines [19]. Based on the observations that reduced FGFR1 in the myocardium from diabetic mice (Figure S1), a cytokine array was performed on these hearts that revealed a significant increase in pro-inflammatory mediators ($q < 0.05$), including Interferon alpha (IFNα), Interferon beta (IFNβ), C-reactive protein (CRP), Interleukin-1 beta (IL-1β), and tumor necrosis factor alpha (TNF-α), accompanied by a reduction in anti-inflammatory cytokines, such as Interleukin-10 (IL-10), Interleukin-11 (IL-11), and endostatin (Figure 1E). These results mirrored the elevated mRNA levels of pro-inflammatory cytokines, including *IL1B*, *CRP*, *TNFA*, Interleukin-6 (*IL6*), *IFNA*, and *IFNB* in human diabetic failing hearts (Figure 1F). More convincingly, TNF-α protein levels were also significantly increased in cardiac tissue from human HF patients (Figure 1G), aligning with altered TNF signaling identified through RNA sequencing in diabetic mouse hearts (Figure 1D). Collectively, these findings lead to a hypothesis that FGFR1 loss could be associated with a pro-inflammatory state in diabetic HF.

2.2. Cardiomyocyte FGFR1 Deletion Aggravates Cardiac Inflammation and Dysfunction Under Diabetic Stress

To investigate whether cardiac FGFR1 loss causes or promotes myocardial inflammation, CM-specific *Fgfr1* knockout mice ($FGFR1^{cKO}$) [20] were subjected to a 10-week regimen of chow or diabetic stress (Figure 2A). To compare the floxed littermate controls ($FGFR1^{Flox}$) under diabetic stress, cardiac performance and phenotypes were assessed to determine the consequences of FGFR1 loss in CMs. First, the induction of diabetes was confirmed by elevated fasting blood glucose and impaired glucose tolerance (Figure S2A,B). Of note, these metabolic parameters were comparable between diabetic $FGFR1^{cKO}$ and $FGFR1^{Flox}$ mice (Figure S2A,B), indicating that the observed cardiac phenotypic differences between $FGFR1^{Flox}$ and $FGFR1^{cKO}$ mice were not secondary to systemic metabolic differences. Importantly, at this stage, FGFR1 protein levels remained unchanged in the control hearts, enabling a direct assessment of FGFR1 loss independent of diabetic stress (Figure S3).

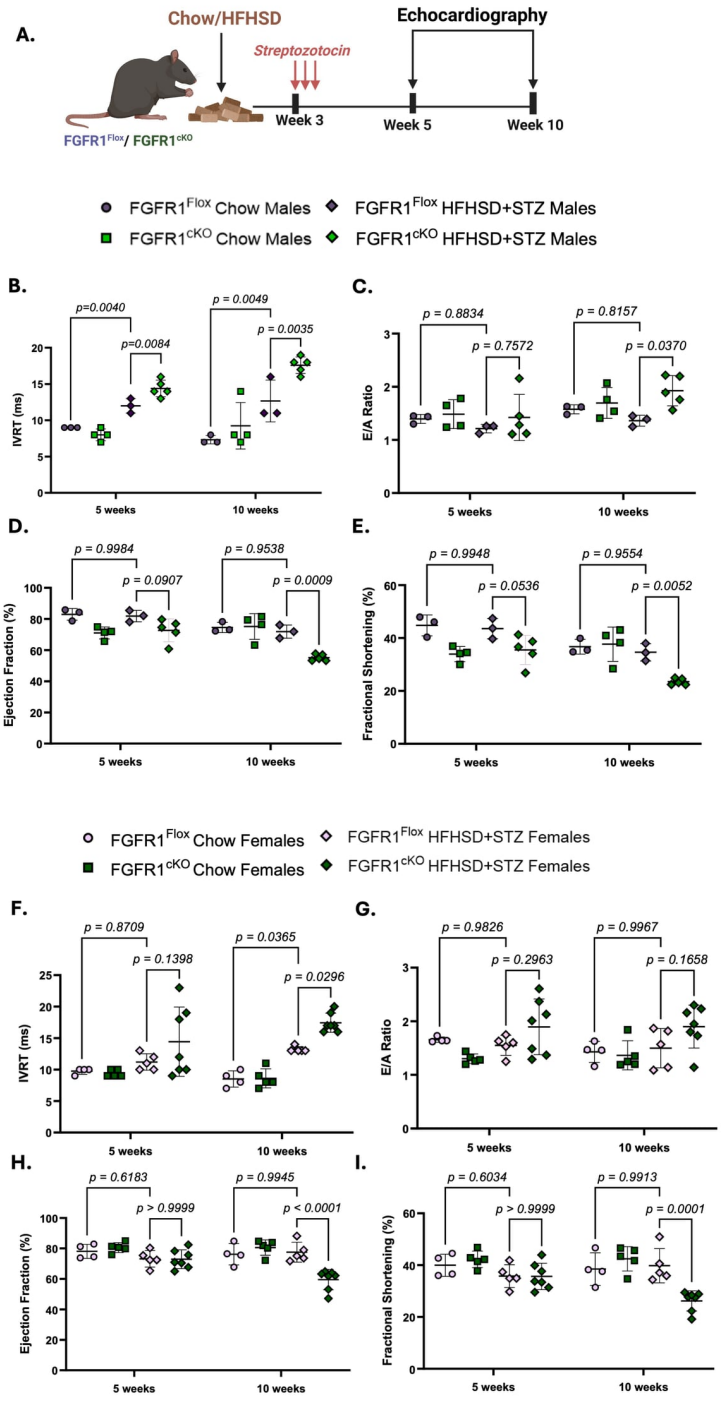

Figure 2. Cardiomyocyte FGFR1 deficiency accelerates cardiac dysfunction in diabetes. (**A**) Experimental design. FGFR1^{Flox} and FGFR1^{cKO} mice were subjected to 10 weeks of chow or high-fat, high-sucrose diet combined with streptozotocin (HFHSD + STZ) to induce diabetic stress. The same mice underwent echocardiography at week 5 and were maintained until the 10-week endpoint. (**B**–**E**) Cardiac functional parameters in male FGFR1^{Flox} and FGFR1^{cKO} littermates after 5 and 10 weeks of chow feeding or HFHSD + STZ treatment. (**B**) Isovolumic relaxation time (IVRT). (**C**) Ratio of early (**E**) to late (**A**) ventricular filling velocities (E/A Ratio). (**D**) Percentage of left ventricular ejection fraction, (**E**) Percentage of left ventricular fractional shortening (n = 3–5 male mice/group). (**F**–**I**) Cardiac functional parameters in female FGFR1^{Flox} and FGFR1^{cKO} littermates following 5- and 10-week of chow feeding or HFHSD + STZ. (**F**) IVRT. (**G**) E/A Ratio. (**H**) Percentage of left ventricular ejection fraction. (**I**) Percentage of left ventricular fractional shortening (n = 4–7 female mice/group). Data are presented as the mean ± SEM. Statistical significance (p values shown in the panel) was assessed using ordinary two-way ANOVA followed by Šidák multiple comparisons (**B**–**I**).

Two-dimensional echocardiography revealed that CM-specific FGFR1 deficiency exacerbated cardiac dysfunction in both male and female mice under diabetic stress (Tables S1 and S2). Diastolic function was indicated by isovolumic relaxation time (IVRT) (Figure 2B,F) and the ratio of peak blood flow velocity from left ventricular relaxation in early diastole (E wave) to that in late diastole (A wave) (E/A ratio) (Figure 2C,G), while systolic function was reflected by ejection fraction (Figure 2D,H) and fractional shortening (Figure 2E,I). In male mice, FGFR1 deficiency resulted in an earlier onset of diastolic dysfunction, with IVRT significantly prolonged after 5 weeks of diabetic stress and further worsened by 10 weeks. In addition, the E/A ratio was significantly increased in diabetic FGFR1^{cKO} mice compared with the diabetic floxed controls. Notably, diabetic male FGFR1^{Flox} mice also exhibited prolonged IVRT relative to chow-fed mice at both time points, suggesting that FGFR1 loss amplifies diabetic stress-induced diastolic dysfunction (Table S1). In female mice, impaired diastolic function manifested later, with a significant prolongation of IVRT observed after 10 weeks of diabetic stress in both FGFR1^{Flox} and FGFR1^{cKO} mice (Table S2). In contrast, reduced systolic function followed a similar pattern in both sexes, with ejection fraction and fractional shortening significantly reduced in diabetic FGFR1^{cKO} mice of both sexes under diabetic stress (Tables S1 and S2). These findings suggest an increased vulnerability to detrimental cardiac phenotypes in the absence of FGFR1 signaling in CMs under diabetic conditions.

RNA sequencing was performed on hearts from diabetic mice, showing 299 altered genes ($P_{adj.} < 0.10$) in FGFR1^{cKO} mice compared with floxed mice. Pathway enrichment and GO analysis ($p < 0.05$) revealed augmented inflammatory signaling in FGFR1^{cKO} mice (Figure 3A,B and Figure S4). Consistently, diabetic FGFR1^{cKO} hearts exhibited increased CD86^{+} macrophages (Figure 3C) and decreased CD206^{+} macrophages (Figure 3D), indicative of augmented pro-inflammatory macrophage activity. Pathway analysis further identified altered phosphoinositide 3-kinase/protein kinase B (PI3K/AKT) signaling in FGFR1-deficient hearts (Figure 3A). Given that AKT is a potential downstream effector of FGFR1 [21,22], we evaluated its phosphorylation in the myocardium in response to FGFR1 disruption under diabetic conditions. FGFR1 deficiency reduced the phosphorylation of AKT at serine 473 (Ser473) (Figure 3E) in the diabetic heart. On the other hand, TNF-α, previously observed to be elevated in human diabetic hearts (Figure 1F,G), was increased in diabetic FGFR1^{cKO} hearts at both protein and transcript levels (Figure 3F,G), which is also in agreement with RNA-sequencing findings showing increased TNF-related transcriptional pathways in FGFR1^{cKO} hearts (Figure 3A). Correspondingly, expression of the TNF-α transcriptional regulator, NF-κB, was elevated in FGFR1-deficient hearts (Figure 3E). Transcript analyses also confirmed the upregulation of key pro-inflammatory markers, including *Il1b*, *Crp*, *Ifna*, and *Ifnb* (Figure 3F), consistent with human diabetic failing hearts (Figure 1F). Collectively, these findings demonstrate that CM-specific deletion of FGFR1 exacerbates cardiac inflammation and dysfunction under diabetic conditions, likely via the suppression of AKT signaling and elevation of NF-κB-mediated TNF-α.

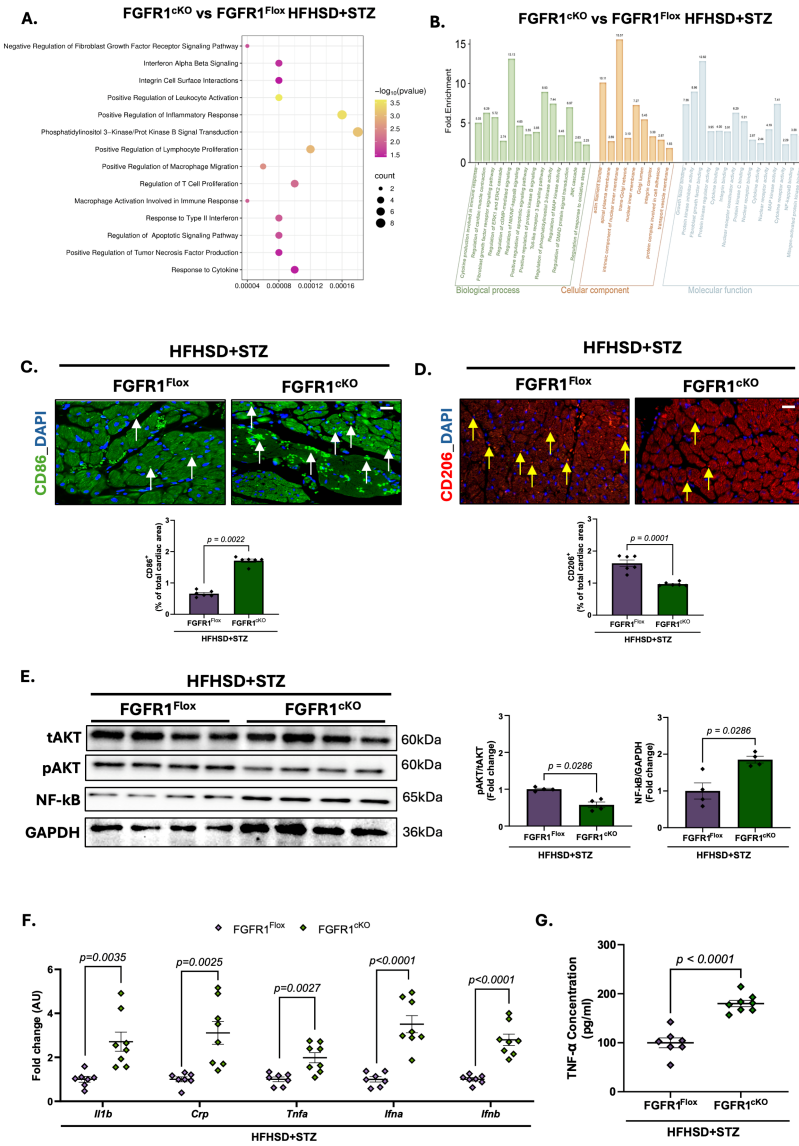

Figure 3. Cardiomyocyte-specific FGFR1 knockout increases myocardial inflammation. (**A**) Gene Ontology (GO) and Reactome pathway enrichment analyses of 299 differentially expressed genes ($P_{adj.} < 0.1$) identified by RNA sequencing from FGFR1^{cKO} hearts compared to FGFR1^{Flox} littermates under high-fat, high-sucrose diet combined with streptozotocin (HFHSD + STZ) stress ($n = 4$ hearts from both sexes/group). (**B**) GO annotation of altered pathways grouped into biological process (green), cellular component (orange), and molecular function (blue). (**C**,**D**) Immunofluorescent co-staining of cardiac tissue from FGFR1^{Flox} and FGFR1^{cKO} mice showing (**C**) CD86^{+} staining (green, white arrows) and (**D**) CD206^{+} staining (red, yellow arrow) with nuclear DAPI (blue) and quantification of CD86^{+} and CD206^{+} areas ($n = 6$ hearts from both sexes/group; scale bar = 20 µm). (**E**) Representative immunoblots and quantification of total AKT (tAKT), phosphorylated AKT (pAKT, Ser473), and NF-κB p65 in hearts from diabetic FGFR1^{Flox} and FGFR1^{cKO} mice ($n = 4$ hearts from both sexes/group). GAPDH was used as the loading control. (**F**) Quantitative PCR analysis of *Il1b*, *Crp*, *Tnfa*, *Ifna*, and *Ifnb* transcripts in mouse diabetic hearts ($n = 7$ mice for FGFR1^{Flox} group, 8 for FGFR1^{cKO} group). Each gene was analyzed separately, with expression normalized to 18S rRNA and expressed as fold change relative to the FGFR1Flox control group. (**G**) TNF-α protein levels measured by ELISA in diabetic FGFR1^{cKO} hearts compared to FGFR1^{Flox} controls ($n = 7$ mice for FGFR1^{Flox} group, 8 for FGFR1^{cKO} group). Data are presented as the mean ± SEM. Statistical significance (p values shown in the panel) was assessed using the Mann–Whitney U test (**C**,**E**) or unpaired t-test (**D**,**F**,**G**).

2.3. FGFR1 Loss Promotes STING Translocation to the Golgi and TNF-α Production Through Suppression of AKT

Next, we used primary neonatal rat cardiomyocytes (NRCMs) as the in vitro model to delineate how reduced FGFR1 signaling in CMs drives inflammation under diabetic stress. FGFR1 was knocked down in cells using its si*RNA* (si*Fgfr1*), followed by 8 h of diabetes-like stress induced by high fatty acids (500 μM palmitic acid conjugated to BSA) and high glucose (25 mM). This time point was selected because endogenous FGFR1 protein levels were unchanged, allowing for an assessment of gene-specific rather than stress-mediated effects (Figure S5). Conditioned media from NRCMs were subsequently used to culture THP-1 cells following differentiation by phorbol 12-myristate 13-acetate (PMA). Since macrophages are key mediators of cardiac inflammation and likely respond to paracrine signals from stressed CMs, macrophage polarization in response to different conditioned media was evaluated by flow cytometry (Figure 4A). $CD86^+$ and $CD206^+$-stained populations were defined (Figure S6A,B), followed by gating to include single, viable cells (Figure S6C). Macrophages exposed to this conditioned medium exhibited an increase in the ratio towards the M1 (CD86-positive cell ratio) phenotype with reduced M2 (CD206-positive cell ratio) polarization (Figures 4B,C and S7).

Consistent with the observation in heart tissues (Figure 3E), FGFR1 knockdown reduced AKT phosphorylation at Ser473 in NRCMs under high-fatty acid and high-glucose conditions (Figure 4D). STING is a key adaptor of innate inflammatory signaling, activating downstream NF-κB-dependent cytokine production. Its translocation from the ER to the Golgi is a critical step for triggering NF-κB signaling, leading to the production and release of pro-inflammatory cytokines, including TNF-α [23–25]. Given that AKT may negatively regulate STING signaling [24], we examined STING localization under diabetes-like stress. In FGFR1-knockdown CMs, STING showed enhanced translocation from the ER to the cis-Golgi compartment (Figure 4E) under diabetes-like stress. As a result, NF-κB (p65) expression in the nuclei (Figure 4F) was elevated, accompanied by increased *Tnfa* transcript levels (Figure 4G). Following this, conditioned media collected from FGFR1-knockdown NRCMs exposed to diabetic stress showed a significant increase in TNF-α levels compared with negative-control siRNA-transfected NRCMs (Figure 4H), indicating more production and secretion of TNF-α due to FGFR1 loss. Notably, STING Golgi translocation was reduced by an AKT activator, SC-79, in FGFR1-deficient NRCMs (Figure S8), supporting that FGFR1 loss induced STING activation due to suppressed AKT. Together, these findings establish that FGFR1 deficiency restrains AKT phosphorylation, allowing STING to translocate to the Golgi and become activated in CMs under diabetic stress. Activated STING then drives NF-κB signaling, resulting in increased TNF-α secretion and enhanced M1 macrophage-mediated inflammatory responses.

To further test whether STING is the key contributor of FGFR1 loss-induced cardiac inflammation, FGFR1-knockdown NRCMs were subjected to diabetic-like stress in the presence or absence of a STING-specific inhibitor, H-151. Conditioned media from these cells were then applied to THP-1 cells after priming with PMA to assess polarization by flow cytometry (Figure 5A). H-151 treatment markedly attenuated NF-κB nuclear distribution (Figure 5B) despite FGFR1 loss, indicating decreased NF-κB. As a result, FGFR1 deficiency-induced *Tnfa* transcript levels (Figure 5C) and TNF-α secretion under diabetic stress were attenuated by H-151 (Figure 5D). Importantly, macrophages exposed to conditioned media obtained from FGFR1-knockdown NRCMs pretreated with H-151 exhibited a shift toward the M2-like phenotype ($CD206^+$); conversely, M1-like ($CD86^+$) macrophages were reduced following exposure to such media (Figure 5E–G). Taken together, these results identify STING signaling as a mediator linking FGFR1 loss to elevated cytokines. Specifically, the pharmacological inhibitor of STING effectively suppresses the paracrine effects of

inflammation between FGFR1-loss in CMs and pro-inflammatory macrophages under diabetic stress.

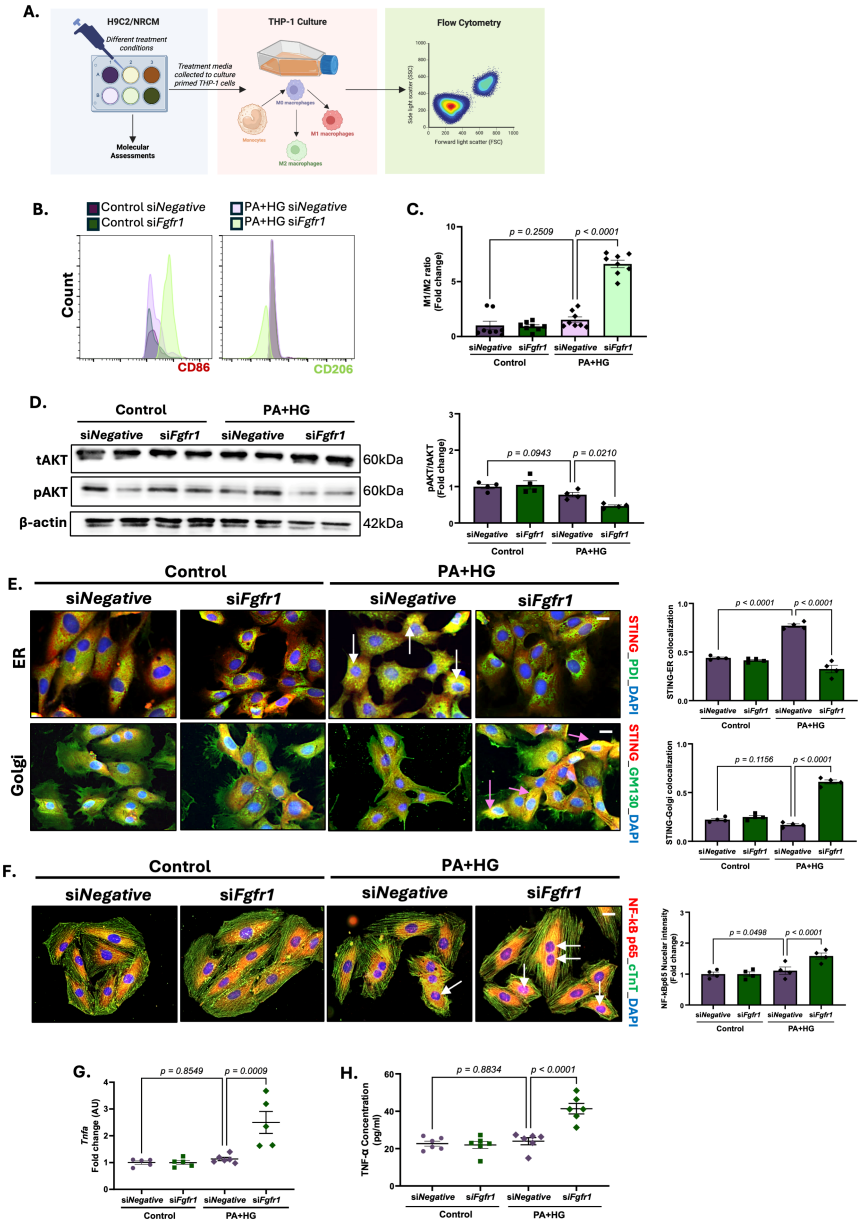

Figure 4. FGFR1 knockdown induces inflammatory changes under diabetes-like stress in a paracrine manner. (**A**) Experimental design. Neonatal rat cardiomyocytes (NRCMs) were transfected with si*RNA* targeting FGFR1 (si*Fgfr1*) and exposed to palmitic acid (PA; 500 µM) and high glucose (HG; 25 mM) for 8 h. The conditioned media from NRCMs were subsequently applied to primed Tohoku Hospital Pediatrics-1 (THP-1) to evaluate macrophage polarization by flow cytometry. (**B**) Combined histograms from flow cytometry showing $CD86^+$ (left) and $CD206^+$ (right) THP-1-derived macrophages cultured in conditioned media from NRCMs subjected to various treatments. (**C**) M1/M2 ratio calculated from the $CD86^+$ and $CD206^+$ macrophage populations under the same treatment conditions ($n = 8$ independent experiments for all groups). (**D**) Representative immunoblots and quantification of total AKT and phosphorylated AKT (Ser473) in FGFR1 knockdown NRCMs using si*Fgfr1* under PA + HG stress ($n = 4$ biological replicates/group). pAKT/AKT ratio was quantified. Beta-actin (β-actin) was used as the loading control. (**E**) Immunofluorescent co-staining from si*Fgfr1* treated NRCMs under control or PA + HG conditions showing STING (red) with DAPI (blue) and either an endoplasmic reticulum marker (PDI; top; green) or cis-Golgi marker (GM130; bottom; green). White arrows represent endoplasmic reticulum localized STING while pink arrows represent

cis-Golgi-localized STING (scale bar = 20 µm). Quantification of Pearson correlation coefficient for colocalization of STING and ER and Manders' coefficient for colocalization of STING and Golgi. Each plotted point represents the mean of 4 images from one independent experiment Golgi (n = 4 independent experiment/group). (**F**) Representative immunofluorescent images showing nuclear NF-κB (red), cTnT (cardiac troponin T; green) and DAPI under similar conditions. Cell-level measurements were averaged within each independent experiment, and each plotted point represents one experimental mean of 10 cells (n = 4 independent experiments/group; scale bar = 20 µm). White arrows represent nuclear localized NF-κB. (**G**) Quantitative PCR analysis of *Tnfa* in NRCMs under the indicated conditions (n = 5–6 samples obtained from independent experiments/group). (**H**) ELISA quantification of secreted TNF-α in conditioned media from FGFR1-knockdown NRCMs exposed to PA + HG (n = 6 samples obtained from independent experiments/group). Data are presented as the mean ± SEM. Statistical significance (p values shown in the panel) was assessed using ordinary two-way ANOVA followed by Šidák multiple comparisons (**C**,**D**,**E**–**H**).

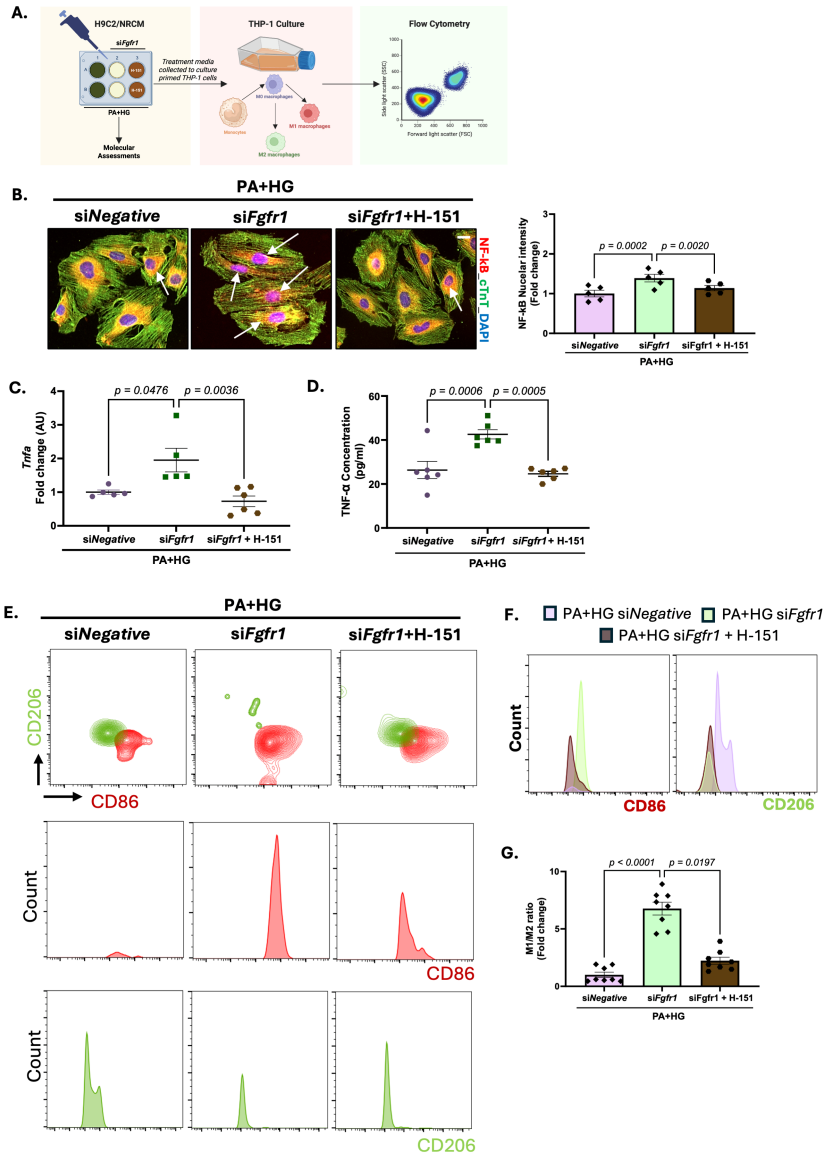

Figure 5. FGFR1 knockdown-induced inflammatory responses are reversed by STING inhibition. (**A**) Experimental design. Neonatal rat cardiomyocytes (NRCMs) were transfected with si*RNA* targeting FGFR1 (si*Fgfr1*) and exposed to palmitic acid (PA; 500 µM) and high glucose (HG; 25 mM) for 8 h in the presence or absence of STING inhibitor, H-151. Conditioned media from NRCMs were subsequently applied to primed Tohoku Hospital Pediatrics-1 (THP-1)-derived macrophages to evaluate macrophage

polarization by flow cytometry. (**B**) Representative immunofluorescent images showing nuclear NF-κB (red), cTnT (cardiac troponin T; green) and DAPI in FGFR1 knockdown NRCMs under PA + HG stress with or without H-151 treatment. Cell-level measurements were averaged within each independent experiment, and each plotted point represents one experimental mean of 10 cells ($n = 5$ independent experiments/group; scale bar = 20 μm). White arrows represent nuclear localized NF-κB. (**C**) Quantitative PCR analysis of *Tnfa* in NRCMs under the indicated conditions ($n = 5$–6 samples obtained from independent experiments/group). (**D**) ELISA quantification of secreted TNF-α in conditioned media from NRCMs subjected to the same treatments ($n = 6$ biological replicates/group). (**E**) Representative flow cytometry contour plots (top) and corresponding histograms (bottom) showing macrophage polarization in response to conditioned media from NRCMs subjected to different treatments. (**F**) Combined histograms depicting $CD86^+$ (left) and $CD206^+$ (right) THP-1-derived macrophages cultured in conditioned media from NRCMs under various treatments. (**G**) M1/M2 ratio calculated from the $CD86^+$ and $CD206^+$ macrophage populations under the same treatment conditions ($n = 8$ samples obtained from independent experiments/group). Data are presented as the mean ± SEM. Statistical significance (p values shown in the panel) was assessed using ordinary one-way ANOVA followed by Holm–Šidák multiple comparisons (**B**,**D**) and Kruskal–Wallis test followed by Dunn's multiple comparisons (**C**,**G**).

2.4. Reinstating FGFR1 Ameliorates Cardiac Inflammation and Dysfunction Under Diabetic Stress

As previously demonstrated, 10 weeks of diabetic stress induced cardiac inflammation and dysfunction in $FGFR1^{cKO}$ mice, establishing them as a model for diabetic HF. To determine whether restoration of FGFR1 in a diseased condition could reverse these deficits, $FGFR1^{cKO}$ mice subjected to 5 weeks of HFHSD combined with STZ were treated with cardiac-specific FGFR1 overexpression using an adeno-associated virus serotype 9 (AAV9) vector driven by cardiac troponin T (cTnT) promoter (AAV9-*Fgfr1*) [20] (Figure 6A). Reinstating FGFR1 in CMs significantly reversed FGFR1 deficiency-induced diastolic dysfunction (Figure 6B,C,F,G) and systolic dysfunction (Figure 6D,E,H,I) in both male and female mice under diabetic stress (Tables S3 and S4), as evidenced by reduced IVRT, normalization of the E/A ratio, and improved ejection fraction and fractional shortening. These data suggest a therapeutic potential of FGFR1 maintenance in improving cardiac dysfunction.

Furthermore, cytokine array-determined cytokine profiling revealed a significant reduction in pro-inflammatory cytokines, such as TNF-α, IL-1β, IL-6, IFNα, accompanied by an increase in anti-inflammatory cytokines like endostatin, progranulin, and transforming growth factor beta (TGFβ) in FGFR1-maintained myocardium (Figure 7A). Further GO pathway enrichment analyses of these 39 significantly altered inflammatory cytokines ($q < 0.05$) confirmed the attenuation of inflammatory pathways ($p < 0.05$) by FGFR1 maintenance (Figure 7B and Table S3). Consistent with these findings, FGFR1 reinstatement reduced $CD86^+$ macrophages and increased $CD206^+$ macrophages (Figure 7), reflecting a likely shift toward the polarization to anti-inflammatory macrophage subtype. GO pathway analyses also showed rescued PI3K/AKT signaling (Figure 7B), corroborated by enhanced AKT phosphorylation at Ser473 and reduced NF-κB expression in FGFR1-restoring hearts despite ongoing diabetic stress (Figure 7E). Correspondingly, both TNF-α transcript levels and protein expression were reduced by FGFR1 reinstatement (Figure 7F,G), accompanied by the downregulation of other key pro-inflammatory mediators, including *Il1b*, *Crp*, *Ifna*, and *Ifnb* (Figure 7F). Together, these findings identify FGFR1 as a protective regulator that mitigates pro-inflammation in diabetic hearts by suppressing TNF-α-mediated paracrine signaling (Figure 8).

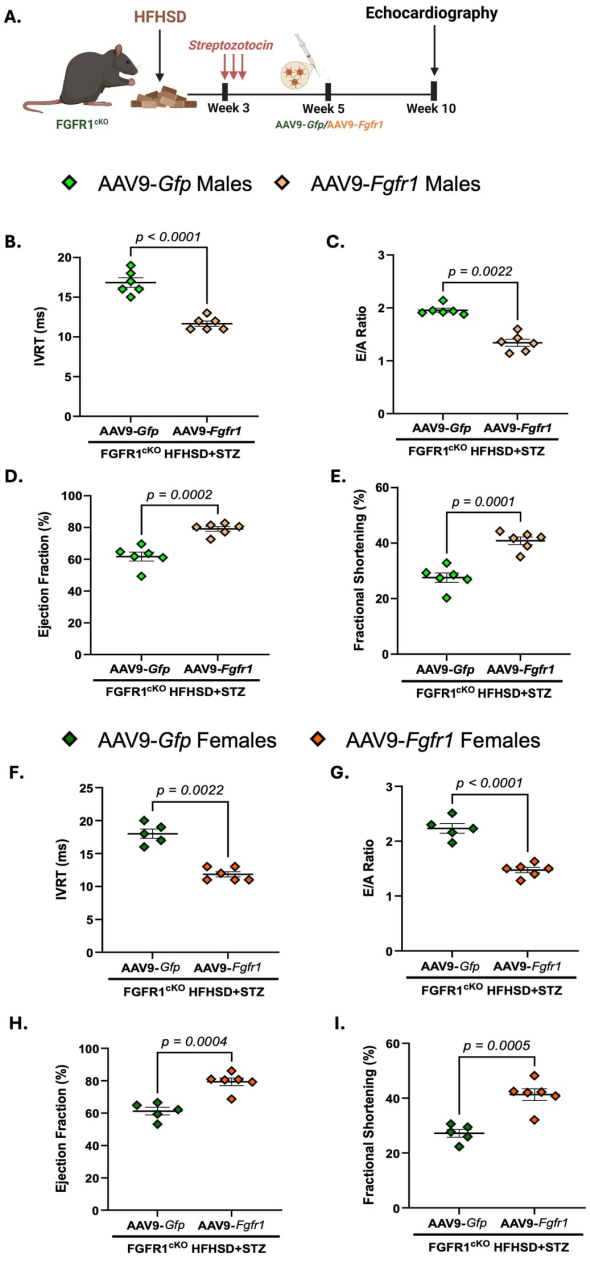

Figure 6. Cardiac FGFR1 restoration ameliorates cardiac dysfunction in FGFR1^{cKO} mice under diabetic stress. (**A**) Experimental design. FGFR1^{cKO} mice were subjected to a high-fat, high-sucrose diet combined with streptozotocin (HFHSD + STZ). Mice received a single tail vein injection of AAV9-*Fgfr1* (AAV9-delivery Troponin T promoter-driven *Fgfr1* expression, 1X10^{11} viral particles) at week 5. AAV9-*Gfp* (1X10^{11} viral particles) was injected as a control. Cardiac function was evaluated at 10 weeks. (**B**–**E**) Cardiac functional parameters in male FGFR1^{cKO} mice following AAV9-*Fgfr1* treatment under diabetic stress. (**B**) Isovolumic relaxation time (IVRT). (**C**) Ratio of peak velocity of blood flow from left ventricular relaxation in early diastole to that in late diastole (E/A Ratio). (**D**) Percentage of left ventricular ejection fraction. (**E**) Percentage of left ventricular fractional shortening (n = 6 male mice/group). (**F**–**I**) Cardiac functional parameters in female FGFR1^{cKO} mice following AAV9-*Fgfr1* delivery under diabetic stress. (**F**) Isovolumic relaxation time (IVRT). (**G**) Ratio of peak velocity of blood flow from left ventricular relaxation in early diastole to that in late diastole (E/A). (**H**) Percentage of left ventricular ejection fraction. (**I**) Percentage of left ventricular fractional shortening (n = 5–6 female mice/group). Data are presented as the mean ± SEM. Statistical significance (p values shown in the panel) was assessed using the Mann–Whitney U test (**C**,**F**) or unpaired t-test (**B**,**D**,**E**,**G**–**I**).

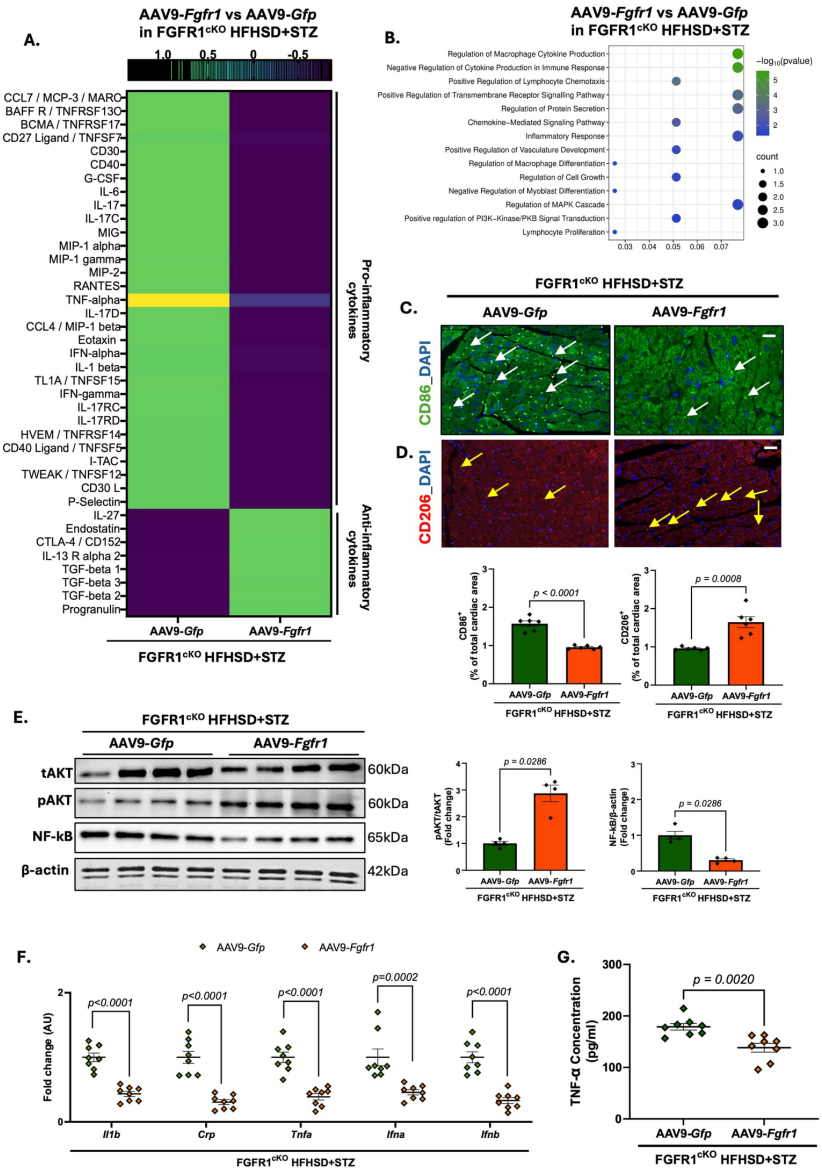

Figure 7. Cardiac-specific FGFR1 overexpression attenuates cardiac inflammatory responses. (**A**) Heatmap of cytokine array analysis showing 39 differentially expressed inflammatory cytokines ($q < 0.05$) in hearts from diabetic FGFR1^{cKO} mice following AAV9-*Fgfr1* treatment versus AAV9-*Gfp* ($n = 2$ pooled samples, each containing 4 hearts of both sexes/group). (**B**) Gene Ontology (GO) pathway enrichment analyses of the 39 differentially expressed cytokines identified by cytokine array shown in panel A. (**C**,**D**) Immunofluorescent co-staining of cardiac tissue from FGFR1^{cKO} mice treated with AAV9-*Fgfr1* or AAV9-*Gfp* showing (**C**) pro-inflammatory CD86$^+$ macrophages (green, white arrows) and (**D**) anti-inflammatory CD206$^+$ macrophages (red, yellow arrows) with nuclear DAPI (blue) and quantification of CD86$^+$ and CD206$^+$ areas ($n = 6$ hearts of both sexes/group; scale bar = 20 µm). (**E**) Representative immunoblots and quantification of total AKT, phosphorylated AKT (Ser473), and NF-κB in hearts from diabetic FGFR1cKO mice treated with AAV9-*Fgfr1* or AAV9-*Gfp* ($n = 4$ hearts from both sexes/group). β-actin was used as the loading control. (**F**) Quantitative PCR analysis of *Il1b*, *Crp*, *Tnfa*, *Ifna* and *Ifnb* transcripts in diabetic FGFR1^{cKO} hearts following FGFR1 overexpression ($n = 8$ mice of both sexes/group). Each gene was analyzed separately, with expression normalized to 18S rRNA and expressed as fold change relative to the AAV9-*Gfp*-treated group. (**G**) TNF-α protein levels measured by ELISA in diabetic FGFR1^{cKO} hearts treated with AAV9-*Fgfr1* or AAV9-*Gfp* ($n = 8$ hearts of both sexes/group). Data are presented as the mean ± SEM. Statistical significance (p values shown in the panel) was assessed using the Mann–Whitney U test (**E**) or unpaired t-test (**C**,**D**,**F**,**G**).

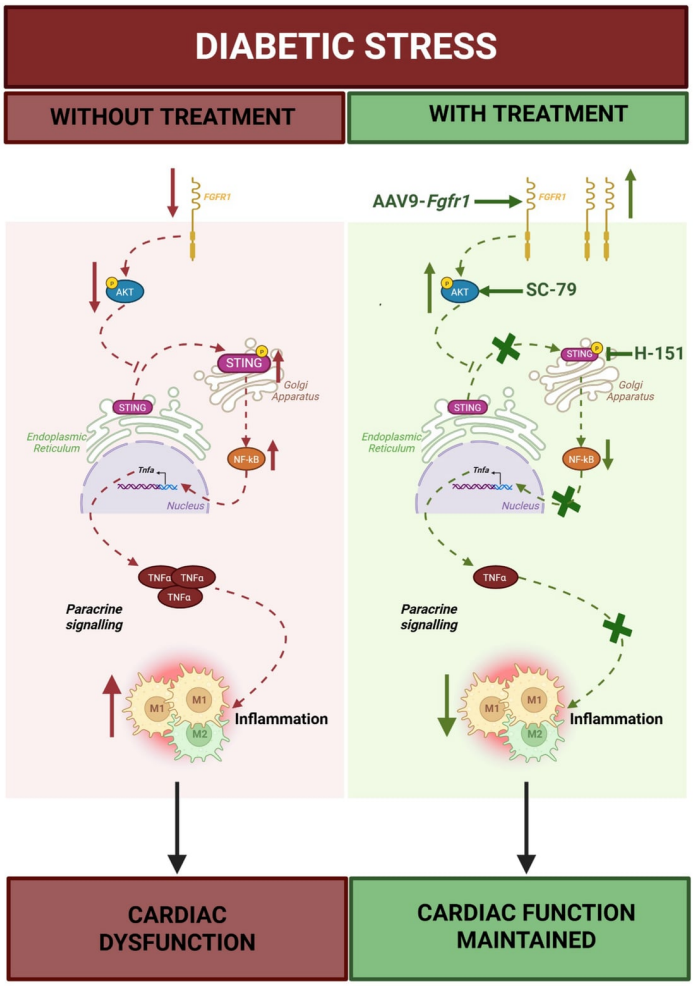

Figure 8. Proposed schematic illustration of FGFR1-STING axis mediating NF-κB/TNF-α dependent in cardiomyocytes. Under diabetic stress, reduced FGFR1 in cardiomyocytes diminishes AKT phosphorylation, contributing to STING translocation from the endoplasmic reticulum (ER) to the Golgi. Subsequently, increased NF-κB is associated with increased TNF-α. Elevated TNF-α is likely one factor driving a shift toward a pro-inflammatory macrophage phenotype, amplifying pathological inflammation within the diabetic myocardium. Various treatments by restoring FGFR1 expression in cardiomyocytes, activating AKT, or pharmacologically inhibiting STING reduces NF-κB and TNF-α release, thereby limiting myocardial inflammation under diabetic stress.

3. Discussion

Our study demonstrated that FGFR1 reduction is associated with elevated inflammation in the myocardium in human and mouse diabetic failing hearts. We found that FGFR1 loss attenuated AKT phosphorylation in CMs. Furthermore, FGFR1 loss-triggered cytokines are regulated by STING signaling-increased NF-κB, subsequently increasing the expression and secretion of TNF-α, which likely promotes macrophage polarization into a pro-inflammatory subtype in a paracrine manner. Conversely, either pharmacological inhibition of STING or the restoration of FGFR1 ameliorates inflammatory events, indicating the therapeutic potential of HF in diabetes by targeting FGFR1 signaling-mediated anti-inflammatory effects.

Chronic myocardial inflammation contributes to the development and progression of HF, and this effect appears to be exacerbated in patients with diabetes. Activated inflammatory pathways and elevated cytokines in the myocardium worsen myocardial dysfunction, independent of coronary artery disease or hypertension. For example, in human end-stage

HF, myocardial TNF-α and IL-6 are increased compared with non-failing hearts [26]. In addition, broad transcriptome profiling from human failing hearts also shows abnormal expression of type I interferon-related genes [27]. Our study demonstrated that inflammatory pathways and cytokine-mediated pathways were altered in diabetic failing hearts. Both human and mouse heart tissues showed higher mRNA levels of pro-inflammatory cytokines, including *CRP*, *TNFA*, *IL1B*, *IFNA*, and *IFNB*, which provides direct evidence that inflammatory cytokines are locally upregulated within the diabetic failing myocardium and supports a pathogenic role for intrinsic myocardial inflammation in the pathogenesis of diabetic HF.

Sex-related differences in inflammation have been studied in patients with HF. For instance, men with higher degrees of inflammation, indicated by serum levels of TNF-α, have a greater risk of HF and cardiac-related events [28]. In patients with coronary heart disease, an increase in circulating IL-6 is associated with higher rates of major adverse cardiovascular outcomes in women [29]. Of note, proteomic analyses of patients with type 2 diabetes and acute coronary syndrome demonstrated that biomarkers related to inflammation are elevated more in women who later experienced HF hospitalization [30], suggesting a difference in systemic inflammation between sexes in distinct clinical contexts. However, the current studies are limited to biomarkers in blood. By demonstrating comparable associations between FGFR1 loss-associated myocardial cytokine levels, such as IFNs, TNF-α, ILs, and HF in both diabetic male and female mice, our study supports targeting local myocardial inflammation as a therapeutically relevant strategy for HF irrespective of sex under diabetic stress.

Extensive research on FGFR1 has focused on cancer, highlighting its signaling function in mediating cell proliferation, migration and invasion through extracellular signal-regulated kinase (ERK) or AKT pathways. Although related tyrosine kinase inhibitors achieve anti-cancer outcomes, they may induce cardiovascular adverse events [31]. This likely highlights the importance of FGFR1 in the heart. Our preliminary observations of altered inflammatory pathways and reduced FGFR1 in the diabetic myocardium prompted us to investigate the potential link between FGFR1 signaling and myocardial inflammatory responses. Loss-of-function studies showed that macrophage-specific FGFR1 knockout or administration of an FGFR1 inhibitor protected the liver from high-fat diet-induced inflammatory responses, which is akin to the phenotype in hepatocytes [32]. In contrast, it is required to inhibit inflammation in endothelial cells [8]. Our previous in vitro study detected that FGFR1 overexpression in myoblasts plays anti-inflammatory roles [19]; however, its function in vivo and the related altered mechanisms upon diabetic stress were not determined. The present loss-of-function and restoration experiments support a protective role for cardiomyocyte FGFR1 in myocardial inflammation under diabetic stress. However, because AAV9-mediated FGFR1 restoration was evaluated in cardiomyocyte-specific FGFR1-deficient mice, this indicated that FGFR1 overexpression can reverse FGFR1 deficient-induced detrimental effects. To evaluate the broader therapeutic potential of FGFR1 overexpression, gain-of-function studies are needed to be performed on wild-type models under prolonged stress of diabetes to closely mimic the clinical disease development process and treatment outcomes.

Since AKT activation correlates with reduced levels of TNF-α, interleukins, and other pro-inflammatory mediators (like NF-κB) that contribute to myocyte damage, we sought to explore the molecular basis underlying FGFR1-mediated suppression of cytokines in CMs. STING functions primarily as a pro-inflammatory signaling hub, amplifying innate immune responses. Golgi-localized STING triggers recruitment and self-phosphorylation of TANK-binding kinase 1 (TBK1) and/or inhibitor of nuclear factor kappa-B kinase epsilon (IKKε) to activate interferon regulatory factor 3 (IRF3) and/or phosphorylate and degrade inhibitor of

kappa B alpha (IκBα), which is the endogenous inhibitor of NF-κB, respectively. Increased IRF3 and/or NF-κB translocate to the nucleus, where they bind the promoter regions of pro-inflammatory genes, including IFNs and TNF-α [9]. Based on our observations that FGFR1 loss increased the levels of NF-κB, IFNs and TNF-α, the current data indicate that FGFR1 is negatively correlated with the STING pathway in CMs under diabetic stress. More importantly, the administration of a STING inhibitor in FGFR1-loss cells attenuated the upregulation of NF-κB p65 nuclear levels and TNF-α production, further supporting STING as at least one of the downstream effectors of FGFR1. On the other hand, STING may also play a distinct role in the heart by inhibiting autophagy [33]; however, the present study does not investigate autophagic events in the models. Although TNF-α may contribute to the conditioned-medium response, its necessity was not directly tested and contributions from other cardiomyocyte-derived soluble factors cannot be excluded. Despite replacement of the treatment medium before conditioned-medium collection, carryover of PA, excess glucose, or H-151 and their direct effects on macrophage responses cannot be excluded. Furthermore, due to lack of CD68 gating, the current analyses did not directly determine the proportion of CD86-positive or CD206-positive macrophages. Although changes in CD86 and CD206 expression suggest alterations in M1- and M2-associated phenotypes, respectively, further studies incorporating macrophage-specific co-staining and quantitative analysis at the single-cell level are warranted to confirm macrophage polarization. However, the reduced M2-associated marker and promoted M1-associated marker expression due to FGFR1 loss can support the shifted macrophage towards an M1-like phenotype of THP-1 cells. Nevertheless, our results not only illustrate, for the first time, FGFR1 signaling effects on STING in CMs, but also provide evidence to reinforce the therapeutic potential of inhibiting STING to treat diabetes-induced HF [34].

In summary, we have provided functional evidence that FGFR1 acts as an anti-inflammatory regulator in the myocardium under diabetic stress, potentially in part through the modulation of AKT–STING signaling.

4. Materials and Methods

4.1. Data and Materials Availability

All data, experimental materials, and protocols can be obtained from the corresponding author upon request for the purpose of replicating the study. The mouse RNA-Seq dataset analyzed in this study has been deposited in ArrayExpress under accession number E-MTAB-16722. Human proteomics data are available in the PRIDE repository under accession number PXD087356.

4.2. Human Samples

Human heart tissue was obtained from de-identified donors through the United Network for Organ Sharing (UNOS). The study was approved by the Institutional Review Board of Baylor College of Medicine for non-human subject research (protocol number H-53940 (30 June 2023). Human heart samples were classified as healthy control samples (no major comorbidities) or heart failure (Table 1). Human hearts were classified according to the following inclusion and exclusion criteria: Normal healthy donors: ejection fraction $>$ 55%; exclusion: (1) history of myocardial infarction, (2) pregnant women, (3) decompensated heart failure, (4) severe kidney disease, (5) asthma or severe chronic lung disease, (6) cardiac pacemaker or implantable defibrillator, (7) cerebral aneurysm clip, (8) neural stimulator, and (9) history of diabetes. Heart failure donors: inclusion: (1) impaired relaxation (average E/E′ $>$ 9), (2) and/or reduced ejection fraction (<40%) history of at least one of these conditions, chronic kidney disease, hypertension or diabetes; exclusion: (1) pregnant women, (2) severe chronic lung disease, (3) cerebral aneurysm clip, and

(4) neural stimulator. For immunofluorescent staining, snap-frozen heart tissues were embedded in OCT embedding matrix and stored at −80 °C. Samples were cut at a thickness of 10 µm using a Leica CM3050S Cryostat microtome (Leica Biosystems Nussloch GmbH, Nussloch, Germany).

Table 1. Demographics and clinical characteristics of heart donors.

Heart	Age	Gender	Ethnicity	Comorbidities
Control				
1	51	Male	Hispanic/Latino	N/A
2	61	Male	Caucasian	N/A
3	61	Female	Caucasian	N/A
4	56	Female	Caucasian	N/A
5	51	Female	Caucasian	N/A
6	61	Male	African American	N/A
7	61	Female	Caucasian	N/A
8	68	Male	Caucasian	N/A
Heart failure (HF)				
1	82	Female	Caucasian	Hypertension, diabetes, chronic kidney disease
2	38	Male	Caucasian	Hypertension
3	65	Female	Caucasian	Coronary artery disease, chronic obstructive pulmonary disease, hypertension, diabetes
4	52	Male	Hispanic	Type II diabetes, chronic heart failure, chronic kidney disease stage 3, Hyperlipidemia, hypertension, non-ischemic cardiomyopathy, depression
5	51	Female	Caucasian	EMR PMHx-anxiety, appendicitis, asthma, Chiari malformation, Edema, hernia inguinal, HTN, HLD, kidney stones, lipoma (R hip), MRSA, peripheral neuropathy (R leg) and vitamin D deficiency. SHx-gastric bypass, C-section, hysterectomy, appendectomy, cholecystectomy, lumbar fusion L5–S1, TLIF and oophorectomy
6	49	Male	Caucasian	Hypertension
7	51	Male	Caucasian	Hypertension
8	48	Female	Caucasian	Myocardial infarction
9	39	Male	Hispanic/Latino	Myocardial infarction, hypertension
10	62	Male	Not reported	Congestive heart failure, myocardial infarction
11	65	Male	Caucasian	Congestive heart failure, hypertension
12	63	Male	Caucasian	Coronary artery disease, chest trauma, hypertension
13	64	Male	Caucasian	Coronary artery disease, chest trauma, hypertension, aortic graft, stent placed for myocardial infarction
14	74	Male	Not reported	Coronary artery disease

4.3. Animal Studies

All animal experiments were conducted in accordance with the United Kingdom Animals (Scientific Procedures) Act 1986 and were approved by the University of Manchester's ethics committee under project licenses PA8E7CA4E and PP0172073. All mice and rats were housed in conventional conditions in the University of Manchester animal facility with food and water provided *ad libitum* in a 12-h light/dark cycle. Pregnant Sprague-Dawley rats were purchased from Envigo (Indianapolis, IN, USA). Fibroblast growth factor receptor 1 (*Fgfr1*) floxed ($Fgfr1^{fl/+}$) mice were purchased from the Jackson Laboratory (strain #007671) and cross-mated with C57BL/6J for 5 generations, followed by mating with transgenic mice expressing Cre under the α-myosin heavy chain promoter (αMHC-Cre) to generate cardiomyocyte-specific *Fgfr1* knockout mice ($FGFR1^{cKO}$). Floxed littermates ($FGFR1^{Flox}$) were used as controls for respective studies. Male and female mice aged 7–8 weeks were used for experiments. In the restoration experiments, cardiac FGFR1 expression was restored in male and female $FGFR1^{cKO}$ mice using adeno-associated virus serotype 9 (AAV9)-mediated gene delivery. A total of 60 mice were used. Sample sizes were based on previous comparable studies, and the numbers of animals in each group were provided in the corresponding figure legends. Animals were randomly assigned to experimental groups, and investigators were blinded to genotype and treatment during data collection and analysis. No animals or samples were excluded from the analyses. Humane endpoints included lethargy, poor gait, blood glucose > 600 mg/dL, dyspnea and body weight loss > 10%. No adverse effects were observed.

Diabetes was induced using a high-fat, high-sucrose diet (HFHSD; 45% of total calories from fat and 20% from sucrose) combined with streptozotocin (STZ). After 2 weeks of HFHSD feeding, mice received intraperitoneal (i.p.) injections of STZ at 40 mg/kg/day for three consecutive days, with continued HFHSD feeding for the designed duration for the respective experimental cohorts.

4.4. Adeno-Associated Viral Delivery of FGFR1 Cardiac-Specific Overexpression

Cardiac-specific *Fgfr1* overexpression was achieved by tail vein injection of adeno-associated virus serotype 9 (AAV9). The AAV9 vector carried mouse *Fgfr1* cDNA (VectorBuilder, Chicago, IL, USA) under the control of the human cardiac troponin T (cTnT) promoter (AAV9-cTnT-m*Fgfr1*-Myc, produced by Boston Children's Hospital) and was delivered at a dose of 1×10^{11} viral genomes per mouse. Control mice received an equivalent dose (1×10^{11} viral genomes per mouse) of AAV9 encoding enhanced *Gfp* under the cTnT promoter (AAV9-cTnT-e*Gfp*). AAV9 was administered at week 5 of HFHSD feeding, and cardiac outcomes were assessed at week 10.

4.5. Metabolic Measurements

Glucose tolerance tests (GTTs) and fasting blood glucose measurements were performed after a 16-h overnight fast. Mice received an intraperitoneal injection of glucose (2 g/kg body weight), and blood glucose levels were measured from the lateral tail vein at the baseline (0 min) and at 30-min intervals up to 120 min post-injection using an Accu-Chek Aviva glucometer (Roche Diagnostics, Rotkreuz, Switzerland).

4.6. Echocardiography

For cardiac function evaluation, mice were anesthetized using a mixture of 2% isoflurane in 100% oxygen delivered at a flow rate of 1.5 L/min. Transthoracic echocardiography was performed using an Acuson Sequoia C256 system to acquire two-dimensional (2D), M-mode, and pulsed-wave (PW) Doppler ultrasound images. Systolic function parameters (FS% and EF%) were calculated based on measurements of the left ventricle (LV) chamber

and wall dimensions. Diastolic function parameters were determined, including the isovolumic relaxation time (IVRT) and the mitral inflow E/A ratio. Additional echocardiographic parameters are detailed in the supplementary tables for each cohort.

4.7. Embedding and Sectioning

Hearts were collected immediately after dissection and fixed in 4% (w/v) paraformaldehyde (PFA) overnight at 4 °C. Subsequently, the samples were washed with PBS for 1 h and dehydrated through a graded ethanol series (50%, 70%, 90%, and 100%) for 2 h each at room temperature. Following clearing in xylene overnight, the hearts were embedded in paraffin. The paraffin blocks were then sectioned at a thickness of 5 µm using a Leica microtome.

4.8. Immunofluorescent Staining on Mouse Paraffin Sections

Paraffin-embedded mouse heart sections were deparaffinized, rehydrated, and subjected to antigen retrieval in sodium citrate buffer (10 mM, pH 6.0) at 95 °C for 20 min, followed by quenching with 50 mM NH_4Cl. Following sample preparation, the heart sections were blocked using 10% (*v*/*v*) normal donkey serum (NDS) + 0.1% (*v*/*v*) Triton X-100 in PBS for 1 h at room temperature. Mouse sections were then incubated with specific primary antibodies against FGFR1, CD86 (Cell Signaling, Danvers, MA, USA, 19589S, 1:50) and CD206 (Proteintech, Rosemont, IL, USA, 60143-1-IG, 1:50) overnight at 4 °C. After washing, the samples were incubated with the corresponding Alexa Fluor 488- or 594-conjugated secondary antibodies (Jackson ImmunoResearch, PA, USA, 711-585-152 and 715-546-151, 1:500) for 1 h at room temperature. Finally, all sections were mounted using ProLong™ Gold Antifade Mountant containing DAPI (Thermo Fisher Scientific, Waltham, MA, USA, P36935) for nuclear visualization. $CD86^+$ and $CD206^+$ areas were quantified in the total cardiac area using ImageJsoftware (v1.54g).

4.9. Immunofluorescent Staining on Human Heart Cryosections

Immunofluorescent staining was performed on frozen human heart cryosections to assess the impact of HF on CD86 and CD206. Human cryosections were fixed in cold acetone and methanol for 20 min and washed with PBS. The heart sections were blocked with 10% (*v*/*v*) NDS for 1 h at room temperature and incubated with specific primary antibodies against CD86 and CD206 overnight at 4 °C. After washing, the samples were incubated with the corresponding Alexa Fluor 488- or 594-conjugated secondary antibodies for 1 h at room temperature. Finally, all sections were mounted using ProLong™ Gold Antifade Mountant containing DAPI for nuclear visualization. $CD86^+$ and $CD206^+$ areas were quantified in the total cardiac area using ImageJ software (v1.54g).

4.10. RNA Extraction and Real-Time Quantitative Polymerase Chain Reaction (RT-qPCR)

Total RNA was extracted from snap-frozen mouse and human heart tissues and neonatal rat cardiomyocytes (NRCMs) using TRIzol reagent (ThermoFisher Scientific) under RNase-free conditions. Prior to extraction, all work surfaces and equipment were decontaminated with RNaseZap (Invitrogen, Waltham, MA, USA) thoroughly to eliminate RNase contamination. A 25-mg sample of heart tissue was minced into small pieces on a Petri dish containing diethyl pyrocarbonate-treated phosphate-buffered saline (DEPC-PBS) and transferred into a homogenizing tube with TRIzol. Homogenization was performed on ice until no visible fragments remained. To isolate RNA, chloroform was added to induce phase separation, followed by isopropanol precipitation and washing with 70% ethanol. The obtained RNA pellet was air-dried and resuspended in RNase-free water containing SUPERase-In RNase inhibitor. Genomic DNA was removed by DNase I treatment (Ther-

moFisher Scientific). RNA concentration and purity were assessed using a NanoDrop spectrophotometer.

Complementary DNA (cDNA) was synthesized from total RNA using the LunaScript reverse transcription kit. Quantitative PCR was performed using 30 ng of cDNA with SYBR Select PCR Master Mix and individual primers (Qiagen, Venlo, The Netherlands) using the Applied Biosystems QuantStudio™ Flex System. The fold change was calculated using the comparative threshold cycle (ΔΔCt) method [35]. Target gene expression was normalized to phosphoglycerate kinase 1 (*PGK1*) for human samples and *18S* ribosomal RNA for mouse and rat samples.

4.11. RNA Sequencing

Total RNA was extracted from mouse heart tissue as described above. RNA quality and integrity were assessed using an Agilent 2100 Bioanalyzer, and library preparation was performed using the TruSeq Stranded mRNA Library Prep Kit (Illumina, San Diego, CA, USA) employing poly(A)-based enrichment of mRNA with the concurrent removal of rRNA according to the manufacturer's instructions [36,37]. Paired-end sequencing was conducted, generating reads of 59 bp in length. Raw sequencing reads were subjected to quality control using FastQC v0.11.3 (http://www.bioinformatics.babraham.ac.uk/projects/fastqc/, accessed on 18 October 2026) and FastQ Screen v0.14.0 (https://www.bioinformatics.babraham.ac.uk/projects/fastq_screen/, accessed on 18 October 2026) to assess read quality and potential contamination. Adapter sequences and low-quality bases were removed using Trimmomatic v0.39 [38]. Reads were trimmed using a sliding window of 4 bp with a mean quality score below Q20 and reads shorter than 35 bp after trimming were discarded. The following Trimmomatic parameters were applied: ILLUMINACLIP:TruSeq3-PE-2.fa:2:30:10, SLIDINGWINDOW:4:20, and MINLEN:35. Filtered reads were aligned to the mouse reference genome (GRCm39/mm39) obtained from the UCSC Genome Browser using STAR v2.7.7a. The genome index was generated using the GENCODE comprehensive mouse gene annotation (vM31), with the sjdbOverhang parameter set to match the read length [39]. Gene-level read counts were generated during alignment using the 'quantMode GeneCounts' option.

Normalization and differential gene expression analysis were performed using DESeq2 v1.34.0 in R v4.1.2 [40]. Log2 fold change shrinkage was applied using the lfcShrink function with the "apeglm" method. For gene changes in response to prolonged diabetes by HFHSD and STZ, differentially expressed genes identified based on adjusted p value < 0.05 and an absolute log2 fold change > 1 were selected for downstream analysis. On the other hand, for the comparison of diabetic FGFR1^{cKO} and FGFR1^{Flox} hearts, differentially expressed genes based on an adjusted p value < 0.1 were selected as candidate genes for subsequent pathway analyses. We used $P_{adj.} < 0.1$ as the cutoff to balance the control of false discovery rates and the sensitivity to detect potentially relevant gene changes in this exploratory analysis.

Pathway enrichment analysis was conducted using Enrichr (https://maayanlab.cloud/Enrichr/, accessed on 18 October 2026) and the Reactome 2024 library. Significantly altered pathways ($p < 0.05$, as reported by Enrichr) were used to generate the pathway enrichment dot plots using SRPlot [41].

4.12. Liquid Chromatography–Tandem Mass Spectrometry (LC-MS/MS)

Proteomic analysis of human heart tissue was performed using a tandem mass spectrometry (MS)-based workflow as previously described [19,42]. For sample preparation, protein lysates were generated using an S-Trap-based protocol. Briefly, samples were solubilized in S-Trap solubilization buffer containing 5% (w/v) SDS in triethylammonium bicarbonate and disrupted by acoustic sonication using a Covaris LE220+ system to ensure

efficient protein extraction. Protein concentrations were determined prior to downstream processing. Proteins were subsequently reduced with dithiothreitol and alkylated with iodoacetamide to block cysteine residues. Following reduction and alkylation, samples were acidified and loaded onto S-Trap columns to facilitate detergent removal and protein binding. On-column tryptic digestion was performed according to the manufacturer's instructions. The resulting peptides were eluted, desalted using Oligo R3 resin, and vacuum concentrated prior to liquid chromatography–tandem mass spectrometry (LC-MS/MS) analysis.

Raw MS data were processed using Spectronaut (Biognosys, Schlieren, Switzerland). Protein identification was performed by database searching against the Swiss-Prot human proteome, with both peptide- and protein-level false discovery rates controlled at 1%. Quantitative proteomic datasets generated from this workflow were subsequently used for downstream statistical analysis. Pathway enrichment analysis was performed using Enrichr (https://maayanlab.cloud/Enrichr/, accessed on 18 October 2026) with the Reactome 2024 library. Significantly altered pathways ($p < 0.05$ obtained on Enrichr) were used to generate the pathway enrichment dot plots using SRPlot [41].

4.13. Neonatal Rat Cardiomyocyte (NRCM) Isolation and Culture

NRCMs were prepared from 2–3-day-old Sprague-Dawley male and female rat pups as described [37]. Briefly, pups were culled in accordance with institutional and UK Home Office regulations, hearts were rapidly excised, atria removed and ventricles dissected into small pieces. Ventricular tissue was subjected to sequential cycles of enzymatic digestion (6-min/cycle, 37 °C) in 7 mL of buffer [116 mM NaCl, 20 mM HEPES, 1 mM NaH_2PO_4, 6 mM glucose, 5 mM KCl, 0.8 mM $MgSO_4$, pH 7.4] containing 0.33 U/mL Collagenase A (Roche, Basel, Switzerland, 10103586001) and 50 mg/mL pancreatin (Sigma-Aldrich, Darmstadt, Germany, P3292). After each cycle, cell-containing supernatant was collected into ice-cold stopping medium supplemented with fetal bovine serum (FBS), and fresh digestion buffer was added to the remaining tissue until it was completely dissociated. Combined cell suspensions were filtered through a 70 µm cell strainer and centrifuged (300× g, 5 min, 4 °C). The pellet was resuspended in cardiomyocyte growth medium [80% DMEM, 20% M199, 1% FBS, 100 µg/mL penicillin–streptomycin, 1% fungizone, and 1 µM bromodeoxyuridine] and maintained on laminin (Sigma-Aldrich, L2020) coated plates at 37 °C in a humidified incubator (5% CO_2).

The effects of HFHSD in vivo were mimicked in vitro by treating cells with high glucose (HG; 25 mM) and high palmitic acid (PA; 500 µM) for 8 h. The concentrations of PA and HG used were optimized according to the existing literature, as well as by our lab previously [43]. BSA in low-glucose (5.5 mM) DMEM served as a control. For conditioned-medium experiments, the treatment medium was replaced after 8 h of PA + HG exposure. Cells were cultured for a further 16 h before conditioned medium was collected for the THP-1 macrophage experiments described below.

4.14. Tohoku Hospital Paediatrics-1 (THP-1) Culture

THP-1 cells (ATCC, TIB-202), a human leukemia monocytic cell line, were used to differentiate into macrophages and assess the paracrine effects of FGFR1 signaling on macrophages. The cells were maintained in RPMI Medium 1640 with 0.05 mM β-mercaptoethanol, 10% (v/v) non-heat-inactivated FBS, 100 µg/mL streptomycin, and 100 U/mL penicillin. For flow cytometry analysis, THP-1 cells were seeded in a 25-cm^2 (T25) flask at a density of 100,000 cells/cm^2. Cells were primed with 150 nM phorbol 12-myristate 13-acetate (PMA; P8139, Sigma-Aldrich) for 24 h and then allowed to recover for 24 h. The differentiated cells were then incubated with conditioned media obtained from NRCMs for 24 h before flow cytometry.

4.15. H-151 and SC-79 Treatment

To inhibit STING activation, H-151 (MedChemExpress, Monmouth Junction, NJ, USA, HY-112693) was added to NRCMs at a concentration of 2 μM for 24 h. This concentration and duration were chosen based on previous studies [44].To activate AKT, SC-79 (MedChemExpress, HY-18749) was added to NRCMs at a dose of 10 μM for 8 h in FGFR1 knockdown cells. This dose was selected based on previous literature [45].

4.16. siRNA Knockdown of Fgfr1

For NRCMs, knockdown of *Fgfr1* was achieved using Silencer Select Pre-Designed rat siRNA targeting Fgfr1 (*siFgfr1*, ThermoFisher Scientific, S135014). NRCMs were seeded and cultured to approximately 70% confluence prior to transfection. Cells were transfected using Lipofectamine LTX & Plus Reagent (ThermoFisher Scientific, 15338-100) according to the manufacturer's instructions. Briefly, si*RNA* was diluted in Opti-MEM medium to a final concentration of 100 nM. Lipofectamine Plus reagent was diluted separately in Opti-MEM and incubated with the siRNA solution for 15 min at room temperature. Lipofectamine LTX reagent was then added, gently mixed, and incubated for a further 30 min at room temperature to allow complex formation. The transfection complexes were added dropwise to the cells, which were subsequently incubated at 37 °C for 48 h prior to downstream analyses.

4.17. Flow Cytometry

Flow cytometry analysis was performed on THP-1-derived macrophages, which were incubated with the conditioned media obtained from NRCMs to assess the paracrine inflammatory effects of cardiac FGFR1 signaling. Once THP-1 cells were primed with PMA and treated with conditioned media, approximately 1×10^6 cell suspension in PBS was centrifuged at 1000× *g* for 5 min, and the pellet was resuspended in 100 μL PBS containing Zombie Aqua™ (BioLegend, San Diego, CA, USA, 423101/423102, 1:500) and incubated at room temperature for 30 min. Post centrifugation, the cells were resuspended in eBioscience™ Flow Cytometry Staining Buffer (Thermo Fisher Scientific, 00-4222-26) and recentrifuged at 1000× *g* for 5 min. Cells were blocked with CD16/32 (BioLegend, 101320) for 10 min on ice and then incubated with antibodies against CD86 (M1 macrophage marker) (BioLegend, 1:100) and CD206 (M2 macrophage marker) (BioLegend, 1:100) for 30 min at room temperature in staining buffer. Stained cells were then fixed with 2% (w/v) PFA at room temperature for 30 min and further washed with flow cytometry staining buffer. The cells were finally resuspended in 100 μL flow cytometry staining buffer. All samples were run on BD Biosciences LSRFortessa with BD FACS software v9.0. Single antibody controls using UltraComp eBeads™ compensation beads (ThermoFisher Scientific) were utilized to generate a compensation matrix. Data were acquired utilizing the following channels: CD86 (M1) 640 (780/60), CD206 (M2) 640 (670/30), Zombie Aqua™ (dead cells) 405 (525/50). Data were analyzed using FlowJo v10 software with appropriate gating, and analyses were restricted to single, viable cells. Sample acquisition and data analyses were blinded to treatment allocation.

4.18. Immunofluorescent Staining of Cells

For immunofluorescence staining, cultured NRCMs were washed with PBS following treatments as stipulated in the Section 2 and fixed with cold methanol at 4 °C for 20 min, allowing simultaneous fixation and permeabilization. After fixation, cells were washed with PBS and blocked with 1% (w/v) BSA in PBS for 1 h at room temperature in a humidified chamber to reduce non-specific binding. Cells were then incubated overnight at 4 °C with primary antibodies diluted in 0.5% (w/v) BSA in PBS. To assess subcellular localization,

antibodies against STING (Proteintech, 19851-1-AP, 1:50) were used in combination with endoplasmic reticulum marker PDI (Proteintech, 66422-1-Ig; 1:50) or cis-Golgi markers (GM130, Proteintech, 66662-1-Ig, 1:50) to examine co-localization. In addition, an anti-p65 antibody (Cell Signaling Technology, MA, USA, 8242T; 1:50) was used to assess NF-κB p65 nuclear localization in NRCMs, and an anti-cTnT antibody (Proteintech, 68300-1-Ig; 1:100) was used to identify cardiomyocytes. Following primary antibody incubation, cells were washed three times with 0.5% (w/v) BSA in PBS. Fluorophore-conjugated secondary antibodies (Jackson ImmunoResearch, West Grove, PA, USA, 1:500) were applied for 1 h at room temperature in the dark. After further washing, coverslips were mounted using ProLong™ Gold Antifade Mountant containing DAPI. Immunofluorescence images were acquired using fluorescence microscopy under identical acquisition settings for all experimental groups to enable comparative analysis. NF-κB p65 nuclear localization was quantified and expressed as fold change relative to the control group. STING localization was assessed by co-staining with PDI or GM130. Cell-level measurements were averaged within each independent experiment, and experiment-level means were used for statistical comparisons. The number of independent experiments and cells analyzed per group are specified in the corresponding figure legends.

4.19. TNF-α ELISA

Rat, mouse, and human TNF-α ELISA kits (FineTest, Wuhan, Hubei, China, ER1393, EM0183, and EH0302) were used to measure TNF-α levels in human and mouse tissues as well as in conditioned media from NRCMs. Assays were performed according to the manufacturer's instructions. Tissue lysates with a protein concentration of 1–3 mg/mL were diluted 1:100 in the supplied sample dilution buffer. Briefly, standard or diluted samples were added to the pre-coated 96-well strips (provided) and incubated for 90 min at 37 °C. After washing, 100 µL of the biotin-labeled detection antibody was added and incubated for 60 min at 37 °C. Plates were then washed three times for a minute each, followed by the addition of 100 µL HRP-streptavidin (SABC) working solution and further incubation for 30 min at 37 °C. After five washes, 90 µL of TMB substrate (provided) was added and incubated for 15 min at 37 °C, followed by the addition of 50 µL stop solution. Optical density was measured at 450 nm using a Promega GloMax® Explorer plate reader.

4.20. Cytokine Array

Mouse heart samples from the following groups were analyzed using an L308 mouse cytokine array (RayBiotech, GA, USA, AAM-BLM-1):

- $FGFR1^{Flox}$ HFHSD + STZ vs. $FGFR1^{Flox}$ Chow;
- $FGFR1^{cKO}$ + AAV9-*Fgfr1* HFHSD + STZ vs. $FGFR1^{cKO}$ + AAV9-*Gfp* HFHSD + STZ.

Four mouse heart tissue samples were pooled as one sample, and approximately 100 mg of tissue was homogenized using 1x cell lysis buffer (diluted from 2× cell lysis buffer provided in the kit). The supernatant was centrifuged at 15,000× *g* for 20 min at 4 °C. The samples were purified via centrifugation at 1000× *g* for 3 min. A total of 100 µg of tissue lysates were diluted with 500 µL of labeling buffer (provided in the kit) and biotin-labeled by incubating the samples with 5 µL of labeling reagent (provided) for 30 min on a shaker at room temperature. The antibody array membrane (provided in the kit) was incubated on a shaker with 6 mL of blocking buffer (provided) for 1 h at room temperature. Later, 6 mL of diluted biotinylated samples were added to the membrane to incubate overnight at 4 °C with gentle shaking. The next day, the array was incubated with HRP-conjugated streptavidin for 2 h. Chemiluminescence was visualized by mixing detection buffers C and D (provided) using a ChemiDoc MP Imaging System (Bio-Rad, Hercules, CA, USA) or Carestream BioMax XAR film (F5513-50EA, Kodak, Rochester, NY, USA) in Hypercassette

(Amersham Biosciences, Little Chalfont, UK) to visualize cytokine intensity. Cytokine intensity was measured using the protein array analyzer plugin of ImageStudio. Cytokines altered between the experimental groups ($q < 0.05$) were presented in a heatmap.

4.21. Protein Extraction and Immunoblotting

Total protein lysates were extracted from tissue and cells using Triton lysis buffer [137 mM NaCl, 20 mM Tris, 0.1% (w/v) SDS, 2 mM EDTA, 10% (v/v) glycerol, 1% (v/v) Triton-X, 25 mM glycerophosphate, protease and phosphatase inhibitor cocktail (Merck, Darmstadt, Germany, PPC1010), pH 7.4]. Protein concentration was quantified using the Bradford assay (Bio-Rad, 500-0006). Immunoblotting was performed using approximately 30 µg protein lysates per lane that were denatured in Laemmli buffer and separated by SDS-PAGE, which were later electrophoretically transferred to PVDF membranes. Membranes were blocked for 1 h at room temperature in 5% (w/v) fat-free milk diluted in Tris-buffered saline containing 0.1% Tween-20 (TBS-T) and incubated overnight at 4 °C with primary antibodies against FGFR1 (Santa Cruz Biotechnology, Dallas, TX, USA, sc-57132; 1:1000), NF-κB p65 (Cell Signaling Technology, 8242T; 1:1000), total AKT (Proteintech, 60203-2-Ig; 1:1000), phospho-AKT (Ser473; Cell Signaling Technology, 4060S; 1:1000), GAPDH (Abcam, Cambridge, UK, ab9482; 1:2000), or β-actin (Proteintech, 66009-1-Ig; 1:1000), diluted in 5% (w/v) fat-free milk. After 3 × 10 min washes in TBS-T, membranes were incubated with HRP-conjugated anti-mouse IgG (Proteintech, RGAM001; 1:2000) or anti-rabbit IgG (Cell Signaling Technology, 7074S; 1:1000) for 1 h at room temperature. Chemiluminescent signals were developed using Amersham ECL Prime or Select (RPN2235 and RPN2236) detection reagents and protein bands were visualized via chemiluminescent imaging using the ChemiDoc system (Bio-Rad). Protein band intensities were quantified by densitometric analysis using ImageJ software (v1.54g). Target protein abundance was normalized to the corresponding loading control on the same membrane as specified in the figure legends.

4.22. Imaging of Immunofluorescent Staining

Immunofluorescence images were acquired using a Zeiss Axioimager D2 upright fluorescence microscope (Carl Zeiss Microscopy Deutschland GmbH, Oberkochen, Germany) equipped with a 40×/0.2 Plan-Neofluar objective. Image capture was performed with a Coolsnap HQ2 camera (Photometrics, Tucson, AZ, USA) controlled by Micro-Manager software (v1.4.23). Appropriate bandpass filter sets for DAPI, FITC, and Texas Red were applied to minimize spectral overlap between channels. Acquired images were subsequently processed and analyzed using ImageJ software (v1.54g). Particularly, colocalization of STING with the ER and Golgi markers was quantified in ImageJ using the Coloc 2 plugin. Pearson's correlation coefficient was used to quantify STING–ER colocalization, and Manders' overlap coefficient was used to quantify STING–Golgi colocalization.

4.23. Statistics

Data are presented as bar/dot plots showing the mean ± SEM. Sample sizes represent biological replicates and are detailed in the corresponding figure legends. For datasets with sample size ≥ 5, normality was assessed using the Shapiro–Wilk test. Normally distributed data involving more than two groups were analyzed using ordinary one-way or two-way ANOVA with appropriate post hoc tests (e.g., Tukey or Šidák), as specified in the figure legends. Comparisons between two groups were performed using unpaired two-tailed Student's *t*-tests. When data were non-normally distributed or sample size was <5, the corresponding non-parametric tests (Mann–Whitney U or Kruskal–Wallis with Dunn's post hoc test) were employed. Statistical analyses were performed using GraphPad Prism (version 10), and q or $p < 0.05$ was considered statistically significant.

Supplementary Materials: The following supporting information can be downloaded at: https://www.mdpi.com/article/10.3390/ijms272310609/s1.

Author Contributions: The project was conceived and overseen by W.L. S.R.G. led the experiments. S.R.G., Y.H. and M.F. conducted key experiments and analyses, including data acquisition, analyses, and interpretation. Y.H. and M.F. did major work in manuscript proofreading and revision. Y.H., M.F., N.H.A., C.R., O.F., X.C. and J.Z. all assisted with the experiments. N.H.A. performed the animal experiments. Y.H. performed neonatal rat cardiomyocyte culture. T.W. and S.A. provided guidance and mentorship throughout the study. R.R.E.A. and T.M.A.M. contributed human heart tissue samples, while G.H. assisted with flow cytometry and offered additional mentorship. B.D.K., supported by a British Heart Foundation Personal Chair, also provided financial support for the work. The manuscript was drafted by W.L. and S.R.G., with additional input from N.H.A., O.F., X.C. and J.Z. All authors have read and agreed to the published version of the manuscript.

Funding: This work was mainly supported by the British Heart Foundation (FS/19/70/34650, PG/19/66/34600, FS/PhD/22/29307, PG/22/10904, PG/22/11075, and PG/24/12025 to W.L; BHF Accelerator award AA/18/4/34221 to the University of Manchester) and Manchester FBMH Doctoral Academy Studentship to S.R.G. T.M.A.M. is supported by NIH grants R01HL147921 and P30GM127607, USA Department of Defense grant W81XWH-20-1-0419, and American Heart Association grant 16SDG29950012. The authors also acknowledge NIH grant F32HL149140 (R.R.E.A.). B.D.K. was supported by a BHF Personal chair (CH/13/2/30154).

Institutional Review Board Statement: The Institutional Review Board of Baylor College of Medicine determined that the use of de-identified human heart tissue obtained through the United Network for Organ Sharing did not constitute human subjects research (protocol H-53940, 30 June 2023). The University of Manchester Ethics Committee approved all animal experiments under project licenses PA8E7CA4E (29 September 2020) and PP0172073 (23 September 2025).

Informed Consent Statement: Patient consent was waived due to Human heart tissue was obtained from de-identified donors through the United Network for Organ Sharing (UNOS). The study was approved by the Institutional Review Board of Baylor College of Medicine for non-human subject research (protocol number H-53940 (30 June 2023).

Data Availability Statement: The original contributions presented in this study are included in the article/supplementary material. Further inquiries can be directed to the corresponding author.

Acknowledgments: We gratefully acknowledge the specialist support provided by core facilities at The University of Manchester, whose contributions were integral to this work. We thank the Bioimaging Facility team, Steven Marsden, Peter March, and James Bagnall, for expert guidance in fluorescence microscopy. We are indebted to Andy Hayes and Leo Zeff for support with the RNA sequencing and bioinformatics analyses. We thank Julian Selley, Melissa Kidd and David Knight for their expertise in mass spectrometry and proteomics. We also sincerely thank the Biological Service Facility for their dedicated assistance with animal care and husbandry.

Conflicts of Interest: T.M.A.M. holds equity at Tenaya Therapeutics. All other authors declare no conflicts of interest.

References

1. Palazzuoli, A.; Iacoviello, M. Diabetes leading to heart failure and heart failure leading to diabetes: Epidemiological and clinical evidence. *Heart Fail. Rev.* **2023**, *28*, 585–596. [CrossRef]
2. Li, Y.; Xian, H.; Xu, Y.; Li, W.; Guo, J.; Wan, K.; Wang, J.; Xu, Z.; Zhang, Q.; Han, Y.; et al. The impact of type 2 diabetes mellitus on the clinical profile, myocardial fibrosis, and prognosis in non-ischemic dilated cardiomyopathy: A prospective cohort study. *Cardiovasc. Diabetol.* **2024**, *23*, 48. [CrossRef]
3. Kaur, N.; Guan, Y.; Raja, R.; Ruiz-Velasco, A.; Liu, W. Mechanisms and Therapeutic Prospects of Diabetic Cardiomyopathy Through the Inflammatory Response. *Front. Physiol.* **2021**, *12*, 694864. [CrossRef]
4. Arvunescu, A.M.; Ionescu, R.F.; Cretoiu, S.M.; Dumitrescu, S.I.; Zaharia, O.; Nanea, I.T. Inflammation in Heart Failure-Future Perspectives. *J. Clin. Med.* **2023**, *12*, 7738. [CrossRef]

5. Zhang, R.; Dong, Y.; Sun, M.; Wang, Y.; Cai, C.; Zeng, Y.; Wu, Y.; Zhao, Q. Tumor-associated inflammatory microenvironment in non-small cell lung cancer: Correlation with FGFR1 and TLR4 expression via PI3K/Akt pathway. *J. Cancer* **2019**, *10*, 1004–1012. [CrossRef]
6. Zhao, Y.N.; Liu, Z.D.; Yan, T.; Xu, T.X.; Jin, T.Y.; Jiang, Y.S.; Zuo, W.; Lee, K.Y.; Huang, L.J.; Wang, Y. Macrophage-specific FGFR1 deletion alleviates high-fat-diet-induced liver inflammation by inhibiting the MAPKs/TNF pathways. *Acta Pharmacol. Sin.* **2024**, *45*, 988–1001. [CrossRef]
7. Wang, C.; Ke, Y.; Liu, S.; Pan, S.; Liu, Z.; Zhang, H.; Fan, Z.; Zhou, C.; Liu, J.; Wang, F. Ectopic fibroblast growth factor receptor 1 promotes inflammation by promoting nuclear factor-kappaB signaling in prostate cancer cells. *J. Biol. Chem.* **2018**, *293*, 14839–14849. [CrossRef]
8. Deng, Y.; Huang, X.; Hu, Y.; Zhong, W.; Zhang, H.; Mo, C.; Wang, H.; Ding, B.S.; Wang, C. Deficiency of endothelial FGFR1 signaling via upregulation of ROCK2 activity aggravated ALI/ARDS. *Front. Immunol.* **2023**, *14*, 1041533. [CrossRef]
9. Decout, A.; Katz, J.D.; Venkatraman, S.; Ablasser, A. The cGAS-STING pathway as a therapeutic target in inflammatory diseases. *Nat. Rev. Immunol.* **2021**, *21*, 548–569. [CrossRef]
10. Zhang, Q.; Shen, L.; Ruan, H.; Huang, Z. cGAS-STING signaling in cardiovascular diseases. *Front. Immunol.* **2024**, *15*, 1402817. [CrossRef]
11. Luo, W.; Zou, X.; Wang, Y.; Dong, Z.; Weng, X.; Pei, Z.; Song, S.; Zhao, Y.; Wei, Z.; Gao, R.; et al. Critical Role of the cGAS-STING Pathway in Doxorubicin-Induced Cardiotoxicity. *Circ. Res.* **2023**, *132*, e223–e242. [CrossRef]
12. Zhang, Y.; Chen, W.; Wang, Y. STING is an essential regulator of heart inflammation and fibrosis in mice with pathological cardiac hypertrophy via endoplasmic reticulum (ER) stress. *Biomed. Pharmacother.* **2020**, *125*, 110022. [CrossRef]
13. Wang, L.; Zhang, S.; Liu, H.; Gao, L.; He, L.; Chen, Y.; Zhang, J.; Yang, M.; He, C. STING activation in cardiomyocytes drives hypertrophy-associated heart failure via NF-kappaB-mediated inflammatory response. *Biochim. Biophys. Acta Mol. Basis Dis.* **2024**, *1870*, 166997. [CrossRef]
14. Ma, X.M.; Geng, K.; Law, B.Y.; Wang, P.; Pu, Y.L.; Chen, Q.; Xu, H.W.; Tan, X.Z.; Jiang, Z.Z.; Xu, Y. Lipotoxicity-induced mtDNA release promotes diabetic cardiomyopathy by activating the cGAS-STING pathway in obesity-related diabetes. *Cell Biol. Toxicol.* **2023**, *39*, 277–299. [CrossRef]
15. Yan, M.; Li, Y.; Luo, Q.; Zeng, W.; Shao, X.; Li, L.; Wang, Q.; Wang, D.; Zhang, Y.; Diao, H.; et al. Mitochondrial damage and activation of the cytosolic DNA sensor cGAS-STING pathway lead to cardiac pyroptosis and hypertrophy in diabetic cardiomyopathy mice. *Cell Death Discov.* **2022**, *8*, 258. [CrossRef]
16. Saitoh, T.; Fujita, N.; Hayashi, T.; Takahara, K.; Satoh, T.; Lee, H.; Matsunaga, K.; Kageyama, S.; Omori, H.; Noda, T.; et al. Atg9a controls dsDNA-driven dynamic translocation of STING and the innate immune response. *Proc. Natl. Acad. Sci. USA* **2009**, *106*, 20842–20846. [CrossRef]
17. Taguchi, T.; Mukai, K.; Takaya, E.; Shindo, R. STING Operation at the ER/Golgi Interface. *Front. Immunol.* **2021**, *12*, 646304. [CrossRef]
18. Oduro, P.K.; Zheng, X.; Wei, J.; Yang, Y.; Wang, Y.; Zhang, H.; Liu, E.; Gao, X.; Du, M.; Wang, Q. The cGAS-STING signaling in cardiovascular and metabolic diseases: Future novel target option for pharmacotherapy. *Acta Pharm. Sin. B* **2022**, *12*, 50–75. [CrossRef]
19. Kaur, N.; Gare, S.R.; Ruiz-Velasco, A.; Miller, J.M.; Abouleisa, R.R.E.; Ou, Q.; Shen, J.; Soran, H.; Mohamed, T.M.A.; Liu, W. FGF21/FGFR1-beta-KL cascade in cardiomyocytes modulates angiogenesis and inflammation under metabolic stress. *Heliyon* **2023**, *9*, e14952. [CrossRef]
20. Alatawi, N.H.; Gare, S.R.; Fang, M.; Han, Y.; Fonseka, O.; Zhang, J.; Chen, X.; Abouleisa, R.R.E.; Wang, T.; Abraham, S.; et al. Cardiomyocyte FGFR1 Signaling Attenuates Adverse Ventricular Remodeling and Preserves Cardiac Function. *Biomolecules* **2026**, *16*, 1621. [CrossRef]
21. Dombrowski, C.; Helledie, T.; Ling, L.; Grunert, M.; Canning, C.A.; Jones, C.M.; Hui, J.H.; Nurcombe, V.; van Wijnen, A.J.; Cool, S.M. FGFR1 signaling stimulates proliferation of human mesenchymal stem cells by inhibiting the cyclin-dependent kinase inhibitors p21(Waf1) and p27(Kip1). *Stem Cells* **2013**, *31*, 2724–2736. [CrossRef]
22. Fan, S.; Chen, Y.; Wang, W.; Xu, W.; Tian, M.; Liu, Y.; Zhou, Y.; Liu, D.; Xia, Q.; Dong, L. Pharmacological and Biological Targeting of FGFR1 in Cancer. *Curr. Issues Mol. Biol.* **2024**, *46*, 13131–13150. [CrossRef]
23. Yum, S.; Li, M.; Fang, Y.; Chen, Z.J. TBK1 recruitment to STING activates both IRF3 and NF-kappaB that mediate immune defense against tumors and viral infections. *Proc. Natl. Acad. Sci. USA* **2021**, *118*, e2100225118. [CrossRef]
24. Seo, G.J.; Yang, A.; Tan, B.; Kim, S.; Liang, Q.; Choi, Y.; Yuan, W.; Feng, P.; Park, H.S.; Jung, J.U. Akt Kinase-Mediated Checkpoint of cGAS DNA Sensing Pathway. *Cell Rep.* **2015**, *13*, 440–449. [CrossRef]
25. Jeong, S.H.; Yang, M.J.; Choi, S.; Kim, J.; Koh, G.Y. Refractoriness of STING therapy is relieved by AKT inhibitor through effective vascular disruption in tumour. *Nat. Commun.* **2021**, *12*, 4405. [CrossRef]
26. Bellemare, M.; Bourcier, L.; Iglesies-Grau, J.; Boulet, J.; O'Meara, E.; Bouabdallaoui, N. Mechanisms of diabetic cardiomyopathy: Focus on inflammation. *Diabetes Obes. Metab.* **2025**, *27*, 2326–2338. [CrossRef]

27. Zhuo, J.; Zhong, Y.; Luo, X.; Qiu, S.; Li, X.; Liang, Y.; Wu, Y.; Zhang, X. Heart Failure Is Closely Associated with the Expression Characteristics of Type I Interferon-Related Genes. *Clin. Cardiol.* **2025**, *48*, e70063. [CrossRef]
28. Saleh, Z.T.; Alraoush, A.T.; Aqel, A.A.; Shawashi, T.O.; Chung, M.; Lennie, T.A. Sex Differences in the Association Between Inflammation and Event-Free Survival in Patients with Heart Failure. *J. Cardiovasc. Nurs.* **2022**, *37*, 386–393. [CrossRef]
29. Sullivan, S.; Young, A.; Hammadah, M.; Lima, B.B.; Levantsevych, O.; Ko, Y.A.; Pearce, B.D.; Shah, A.J.; Kim, J.H.; Moazzami, K.; et al. Sex differences in the inflammatory response to stress and risk of adverse cardiovascular outcomes among patients with coronary heart disease. *Brain Behav. Immun.* **2020**, *90*, 294–302. [CrossRef]
30. Razaghizad, A.; Aziz, H.; Zhang, G.K.; Ferreira, J.P.; White, W.B.; Mehta, C.R.; Bakris, G.L.; Zannad, F.; Sharma, A. Pathophysiological Sex Differences in Heart Failure Progression After Acute Coronary Syndrome: Insights From the EXAMINE Trial. *J. Card. Fail.* **2024**, *30*, 767–777. [CrossRef]
31. Ma, Z.; Cao, F.; Liao, M.; Min, R.; Zheng, R.; Sun, X.; Chen, X.; Gong, Y.; Ai, S.; Kang, X. Cardiovascular adverse events associated with epidermal growth factor receptor tyrosine kinase inhibitors in EGFR-mutated non-small cell lung cancer: Systematic review and network meta-analysis. *BMJ* **2025**, *390*, e082834. [CrossRef]
32. Wang, C.; Li, Y.; Li, H.; Zhang, Y.; Ying, Z.; Wang, X.; Zhang, T.; Zhang, W.; Fan, Z.; Li, X.; et al. Disruption of FGF Signaling Ameliorates Inflammatory Response in Hepatic Stellate Cells. *Front. Cell Dev. Biol.* **2020**, *8*, 601. [CrossRef]
33. Xiong, R.; Li, N.; Chen, L.; Wang, W.; Wang, B.; Jiang, W.; Geng, Q. STING protects against cardiac dysfunction and remodelling by blocking autophagy. *Cell Commun. Signal.* **2021**, *19*, 109. [CrossRef]
34. Hu, S.; Gao, Y.; Gao, R.; Wang, Y.; Qu, Y.; Yang, J.; Wei, X.; Zhang, F.; Ge, J. The selective STING inhibitor H-151 preserves myocardial function and ameliorates cardiac fibrosis in murine myocardial infarction. *Int. Immunopharmacol.* **2022**, *107*, 108658. [CrossRef]
35. Livak, K.J.; Schmittgen, T.D. Analysis of relative gene expression data using real-time quantitative PCR and the 2(-Delta Delta C(T)) Method. *Methods* **2001**, *25*, 402–408. [CrossRef]
36. Ruiz-Velasco, A.; Raja, R.; Chen, X.; Ganenthiran, H.; Kaur, N.; hawimel o Alatawi, N.; Miller, J.M.; Abouleisa, R.R.; Ou, Q.; Zhao, X. Restored autophagy is protective against PAK3-induced cardiac dysfunction. *Iscience* **2023**, *26*, 106970. [CrossRef]
37. Ruiz-Velasco, A.; Zi, M.; Hille, S.S.; Azam, T.; Kaur, N.; Jiang, J.; Nguyen, B.; Sekeres, K.; Binder, P.; Collins, L.; et al. Targeting mir128-3p alleviates myocardial insulin resistance and prevents ischemia-induced heart failure. *Elife* **2020**, *9*, e54298. [CrossRef]
38. Bolger, A.M.; Lohse, M.; Usadel, B. Trimmomatic: A flexible trimmer for Illumina sequence data. *Bioinformatics* **2014**, *30*, 2114–2120. [CrossRef]
39. Harrow, J.; Frankish, A.; Gonzalez, J.M.; Tapanari, E.; Diekhans, M.; Kokocinski, F.; Aken, B.L.; Barrell, D.; Zadissa, A.; Searle, S. GENCODE: The reference human genome annotation for The ENCODE Project. *Genome Res.* **2012**, *22*, 1760–1774. [CrossRef]
40. Love, M.I.; Huber, W.; Anders, S. Moderated estimation of fold change and dispersion for RNA-seq data with DESeq2. *Genome Biol.* **2014**, *15*, 550.
41. Tang, D.; Chen, M.; Huang, X.; Zhang, G.; Zeng, L.; Zhang, G.; Wu, S.; Wang, Y. SRplot: A free online platform for data visualization and graphing. *PLoS ONE* **2023**, *18*, e0294236. [CrossRef]
42. Fonseka, O.; Raja, R.; Ross, C.; Gare, S.R.; Zhang, J.; Hille, S.S.; King, K.; Ruiz-Velasco, A.; Kaur, N.; Chen, X.; et al. XBP1s-EDEM2 Prevents the Onset and Development of HFpEF by Ameliorating Cardiac Lipotoxicity. *Circulation* **2025**, *151*, 1583–1605. [CrossRef]
43. Liu, W.; Ruiz-Velasco, A.; Wang, S.; Khan, S.; Zi, M.; Jungmann, A.; Dolores Camacho-Munoz, M.; Guo, J.; Du, G.; Xie, L.; et al. Metabolic stress-induced cardiomyopathy is caused by mitochondrial dysfunction due to attenuated Erk5 signaling. *Nat. Commun.* **2017**, *8*, 494. [CrossRef]
44. Kobritz, M.; Borjas, T.; Patel, V.; Coppa, G.; Aziz, M.; Wang, P. H151, a Small Molecule Inhibitor of Sting as a Novel Therapeutic in Intestinal Ischemia-Reperfusion Injury. *Shock* **2022**, *58*, 241–250. [CrossRef]
45. Zheng, K.; Zhang, Q.; Lin, G.; Li, Y.; Sheng, Z.; Wang, J.; Chen, L.; Lu, H.H. Activation of Akt by SC79 protects myocardiocytes from oxygen and glucose deprivation (OGD)/re-oxygenation. *Oncotarget* **2017**, *8*, 14978–14987. [CrossRef]

Disclaimer/Publisher's Note: The statements, opinions and data contained in all publications are solely those of the individual author(s) and contributor(s) and not of MDPI and/or the editor(s). MDPI and/or the editor(s) disclaim responsibility for any injury to people or property resulting from any ideas, methods, instructions or products referred to in the content.